

POST PRINT

<https://doi.org/10.1016/j.ymben.2018.06.008>

DOI: 10.1016/j.ymben.2018.06.008.

Adelfia Talà, Fabrizio Damiano, Giuseppe Gallo, Eva Pinatel, Matteo Calcagnile, Mariangela Testini, Daniela Fico, Daniela Rizzo, Alberto Sutera, Giovanni Renzone, Andrea Scaloni, Gianluca De Bellis, Luisa Siculella, Giuseppe Egidio De Benedetto, Anna Maria Puglia, Clelia Peano, Pietro Alifano,

Pirin: A novel redox-sensitive modulator of primary and secondary metabolism in *Streptomyces*,

Metabolic Engineering, Volume 48, 2018, Pages 254-268, ISSN 1096-7176,
<https://doi.org/10.1016/j.ymben.2018.06.008>.

(<https://www.sciencedirect.com/science/article/pii/S109671761830051X>)

Pirin: a novel redox-sensitive modulator of primary and secondary metabolism in *Streptomyces*

Adelfia Talà^{a,1}, Fabrizio Damiano^{a,1}, Giuseppe Gallo^{b,c}, Eva Pinatel^d, Matteo Calcagnile^a, Mariangela Testini^a, Daniela Fico^e, Daniela Rizzo^e, Alberto Sutura^{b,c}, Giovanni Renzone^f, Andrea Scalonif, Gianluca De Bellis^d, Luisa Siculella^a, Giuseppe Egidio De Benedetto^e, Anna Maria Puglia^b, Clelia Peano^{d,g,h} and Pietro Alifano^{a*}

^a*Department of Biological and Environmental Sciences and Technologies, University of Salento, Lecce, Italy*

^b*Department of Biological, Chemical and Pharmaceutical Sciences and Technologies (STEBICEF), University of Palermo, Palermo, Italy*

^c*Advanced Technologies Network (ATeN) Center, University of Palermo, Palermo, Italy*

^d*Institute of Biomedical Technologies, National Research Council, Segrate, Italy*

^e*Laboratory of Analytical and Isotopic Mass Spectrometry, Department of Cultural Heritage, University of Salento, Lecce, Italy*

^f*Proteomics & Mass Spectrometry Laboratory, ISPAAM, National Research Council, Naples, Italy*

^g*Institute of Genetic and Biomedical Research, UoS Milan, National Research Council, Rozzano, Milan, Italy*

^h*Humanitas Clinical and Research Center, Rozzano, Milan, Italy*

* Corresponding author. Tel: 0039 0832 298856; Fax: 0039 0832 298626

E-mail address: pietro.alifano@unisalento.it (P. Alifano)

¹These authors contributed equally to this publication and should be considered co-first authors

Abbreviations

2D-DIGE, 2D-differential gel electrophoresis; ACAD, acyl-CoA dehydrogenase; ACT, actinorhodin; ANOVA, analysis of variance; Att/Int, attachment/integration; CHAPS, 3-[(3-cholamidopropyl)dimethylammonio]-1-propanesulfonate; DTT, dithiothreitol; CID, collision-induced dissociation; DCPIP, 2,6-dichlorophenolindophenol; EDTA, ethylenediaminetetracetic acid; ESI, electrospray ionization; ATR-FTIR, attenuated total reflectance - Fourier transform infrared; hPirin, human Pirin; HPLC, high-performance liquid chromatography; IEF, isoelectric focusing; IPTG, isopropyl β -D-1-thiogalactopyranoside; LC, liquid chromatography; LCAD, long-chain acyl-CoA dehydrogenase; LODs, limits of detection; LOQs, limits of quantification; MCAD medium-chain acyl-CoA dehydrogenase; MEP, methylerythritol phosphate; MS, mass spectrometry; NF-I/CTF, nuclear factor I/ CAAT-box transcription factor; NF- κ B, nuclear factor kappa B; PKS, polyketide synthase; PMS, phenazine methosulfate; PMSF, phenylmethylsulfonyl fluoride; PAGE, polyacrylamide gel electrophoresis; (p)ppGpp, guanosine 5'-triphosphate 3'-diphosphate and guanosine 5'-diphosphate 3'-diphosphate; RG1, rapid growth phase 1; RG2, rapid growth phase 2; SCAD, short chain acyl-CoA dehydrogenase; SDS, sodium dodecyl sulfate; SFM, soya flour mannitol; SRM, selected reaction monitoring mode; TAG, triacylglycerols; TES, Tris EDTA buffer saline; vLCAD, very long-chain acyl-CoA dehydrogenase; WS, washing solution; YS, yeast starch.

Abstract

Pirins are evolutionarily conserved iron-containing proteins that are found in all kingdoms of life, and have been implicated in diverse molecular processes, mostly associated with cellular stress. In the present study, we started from the evidence that the insertional inactivation of pirin-like gene SAM23877_RS18305 (*pirA*) by Φ C31 Att/Int system-based vectors in spiramycin-producing strain *Streptomyces ambofaciens* ATCC 23877 resulted in marked effects on central carbon and energy metabolism gene expression, high sensitivity to oxidative injury and repression of polyketide antibiotic production. By using integrated transcriptomic, proteomic and metabolite profiling, together with genetic complementation, we here show that most of these effects could be traced to the inability of the *pirA*-defective strain to modulate beta-oxidation pathway, leading to an unbalanced supply of precursor monomers for polyketide biosynthesis. Indeed, *in silico* protein-protein interaction modeling and *in vitro* experimental validation allowed us to demonstrate that PirA is a novel redox-sensitive negative modulator of very long-chain acyl-CoA dehydrogenase, which catalyzes the first committed step of the beta-oxidation pathway.

KEYWORDS: Actinomycetes; Pirin; Beta-oxidation of fatty acids; Secondary metabolism; Antibiotics.

1. Introduction

Streptomycetes are mycelial soil-dwelling bacteria relevant for their cell cycle and ability to produce a wide array of biologically active secondary metabolites including antibiotics, anticancer agents and immune-suppressants. Genetic manipulation of these bacteria is often labor and time intensive due to their large genome and complex life cycle. Over the past three decades, integrative vectors based on temperate actinophages Φ C31, Φ BT1, R4 and TG1 were among the few valuable tools for their genetic manipulation (Batzl, 2012). These actinophages form lysogens by integrating site-specifically through a unidirectional recombination between the bacteriophage *attP* and specific *attB* sites mapping to conserved regions of the streptomycete chromosome (Smith et al., 2010). The unidirectional nature of the integration and the peculiar features of the attachment/integration (*att/int*) system were exploited to produce stable recombinants not only in streptomycetes but also in other actinomycetes, and even in eukaryotes and archaea (Calos, 2006; D'Argenio et al., 2016; Kieser et al., 2000).

The widely used Φ C31-based vectors integrate into an *attB* site of a Pirin-encoding gene located in close proximity to the chromosomal origin of replication *oriC* site, in a region that contains mainly highly conserved genes (Bentley et al., 2002; Ikeda et al., 2003). Pirin was initially isolated in human (hPirin) as an interactor of the NF- κ B (Wendler et al., 1997). It was later described its ability to form quaternary complexes with Bcl-3 and dimer of NF- κ B on NF- κ B binding sites to promote the transcription of anti-apoptotic genes (Dechend et al., 1999). These findings suggested that hPirin could be involved in transcription regulation or in other nuclear processes, such as DNA replication or repair, although its precise role remains elusive.

Pirins belong to the cupin superfamily, a group of functionally diverse proteins that have a characteristic signature domain comprising two histidine-containing motifs separated by an intermotif region of variable length (Khuri et al., 2001). Like other cupins, Pirins have a metal binding motif. The crystal structure of hPirin revealed that a single Fe(II)/Fe(III) ion is located in

the N-terminal cupin domain, where it is coordinated by three histidine residues and one glutamic acid residue (Pang et al., 2004).

Pirin-encoding orthologs are found in all kingdoms of life. In tomato, hPirin homolog was implicated in programmed cell death (Orzaez et al., 2001), while in *Arabidopsis thaliana* AtPirin1 was involved in the regulation of seed germination and early seedling development (Lapik and Kaufman, 2003). In cyanobacteria, expression of a Pirin-encoding gene was found to be highly induced under severe salt stress and other stress conditions (Hihara et al., 2004). In the nitrifying *Nitrosomonas europaea*, microarray analysis demonstrated a strong up-regulation of a Pirin-encoding gene during phenol exposure (Lauchnor et al., 2011). Adams and Jia (2005) determined the crystal structure of the Pirin-encoding ortholog YhhW from *Escherichia coli*, and provided both structural and biochemical evidences that both hPirin and YhhW may act as 2,3-dioxygenases using the antioxidant quercetin as a substrate. Later on, Soo and colleagues (Soo et al., 2007) showed that a Pirin-encoding ortholog from *Serratia marcescens* regulates pyruvate catabolism by interacting with the pyruvate dehydrogenase E1 subunit. All these studies indicate that Pirin-encoding orthologs play important role in a number of different biological processes, and often associate the cellular function of this group of proteins with stress conditions.

The present study was motivated by the evidence that manipulation of spiramycin-producing strain *Streptomyces ambofaciens* ATCC 23877 by Φ C31-based integrative vector resulted in a significant drop in spiramycin production and some phenotypic changes due to inactivation of the Pirin-encoding gene SAM23877_RS18305 (herein referred to as *pirA*). To get insight into the molecular mechanisms underlying this phenomenon, we have analyzed the transcriptome and proteome of the wild type strain and *pirA*-defective strain. Results were then validated by functional assays. Evidence is provided that *pirA* inactivation leads to dramatic gene expression changes with marked effects on central carbon and energy metabolism, high sensitivity to oxidative injury and repression of polyketide antibiotic production. Most of these effects could be traced to inability of

the *pirA*-defective strain to modulate beta-oxidation pathway with consequences on supply of short chain acyl-CoA precursors (Chan et al., 2009) for polyketide biosynthesis.

2. Materials and methods

2.1. Bacterial strains, media, growth conditions and phenotypic analysis

S. ambofaciens ATCC 23877 was obtained from the American Type Culture Collection (ATCC). The genome sequence of this microorganism was determined (Thibessard et al., 2015). The composition (per liter) of the media used in this study for *S. ambofaciens* growth and manipulation is here reported. Yeast starch (YS) broth: 2 g yeast extract, 10 g soluble starch, (18 g agar in YS agar); SM-II: 15 g dextrose, 10 g soybean flour, 0.5 g $\text{MgSO}_4 \cdot 7 \text{H}_2\text{O}$, 5 g CaCO_3 , 15 g agar; Soya flour mannitol (SFM) agar: 20 g mannitol, 20 g soya flour, 20 g agar. Composition of R2 agar is reported (Kieser et al., 2000). For fermentation experiments, *S. ambofaciens* strains were cultivated in shake flasks at 28 °C on a rotary shaker at 200 rpm as described (Fondi et al., 2017; Calcagnile et al., 2018).

Differences in grey pigmentation of surface mycelium of *S. ambofaciens* strains growing on SM-II agar at different time points were evaluated by reflectance spectrophotometry using a CM-2600d spectrophotometer (Konica Minolta). The measurement area was a circle having a diameter of 6 mm, and the spectral reflectance analysis was carried out at 10 nm intervals between 360 nm and 740 nm. Considering the inhomogeneity of mycelial growth on SM-II agar, the analysis was conducted by positioning the spectrophotometer on 10 distinct points, and values of reflectance were reported as mean \pm standard deviation.

2.2. DNA procedures and construction of plasmids and recombinant strains

S. ambofaciens total genomic DNA was obtained as recently described (Fondi et al., 2017). DNA manipulation in *Escherichia coli* strain DH5 α was performed according to standard procedures (Sambrook and Russell, 2001).

E. coli-Streptomyces spp. shuttle vector plasmid pTYM-18 has been previously described (Onaka et al., 2003). Plasmid pTYM-pirA was obtained by cloning the PCR-amplified region coding for *pirA* into pTYM-18. The *pirA* gene with its promoter region was amplified from *S. ambofaciens* ATCC 23877 genome using the primer pair PirHindIII_F and PirXbaI_R, whose sequence is reported below (*Hind*III and *Xba*I restriction sites are underlined):

PirHindIII_F:5'- GCGGTGTAAAGCTTGACGTGCTGTCAGCCGGGGCCGG- 3'

PirXbaI_R:5'- GCTAGACGTCTAGACCCCACAGGCGGCCGTACGCGACCG-3'

The amplified fragment was digested with *Hind*III and *Xba*I, and the resulting 1162 bp DNA fragment was cloned into pTYM-18 using the *Hind*III and *Xba*I restriction sites of the polylinker.

Plasmids pTYM-18 or pTYM-pirA were introduced into the *S. ambofaciens* strain by conjugation with *E. coli* GM2929/pUB307::Tn7, as described previously (Fondi et al., 2017).

pET-AcdB-V5-His6 and pET-PirA-V5-His6 were constructed as follows. The V5 epitope tag DNA (GGTAAGCCTATCCCTAACCTCTCCTCGGTCTCGATTCTACG) with or without TAA codon stop was cloned into the *Hind*III and *Xho*I sites of pET21b obtaining pET21b-V5 and pET21b-V5-His6, respectively. *acdB* and *pirA* were amplified from *S. ambofaciens* ATCC 23877 genome using the primer pairs AcdB-for/AcdB-rev and PirA-for/PirA-rev (*Nde*I and *Hind*III restriction sites are underlined):

AcdB-for: 5'-AAGCTTCATATGCCTCGCCGATCTCTCAA-3'

AcdB-rev: 5'-GAATTCAAAGCTTGAAGGCCGCTCGTCCAGC-3'

PirA-for 5'-AAGCTTCATATGCCTGCCGTGACCGTCGAG-3'

PirB-rev 5'-GAATTCAAAGCTTGGCCTCGGGCCCCGCCG-3'

The amplified *acdB* DNA fragment was digested with *Nde*I and *Hind*III, and then ligated to *Nde*I and *Hind*III -cleaved pET21b-V5-His6, obtaining the resulting plasmid pET-AcdB-V5/His. The amplified *pirA* DNA fragment upon *Nde*I/*Hind*III digestion was inserted into the *Nde*I- and *Hind*III-cleaved pET21b-V5 or pET21b-V5-His6 obtaining pET-PirA-V5 and pET-PirA-V5-His6, respectively.

2.3. Overproduction and purification of recombinant *AcdB* and *PirA*

Purified recombinant *S. ambofaciens* *AcdB* and *PirA* were obtained by introducing pET-*AcdB*-V5-His6 and pET-*PirA*-V5-His6 into *E. coli* BL21(DE3). Bacteria harboring pET-*AcdB*-V5-His6 or pET-*PirA*-V5-His6 were grown in 50 ml of LB medium supplemented with ampicillin (10 µg/ml) to A600 = 0.6 at 37 °C with shaking (250 rpm). Protein production was induced by addition of 0.4 mM IPTG and incubation of bacteria for 5 h at 37 °C with shaking (250 rpm). His6-tagged recombinant proteins were purified by using the Ni-IMAC resin (Bio-Rad Laboratories) as previously described (Fondi et al., 2017).

2.4. RNA extraction and RNAseq experiments

S. ambofaciens strains were grown in YS medium at 28 °C on a rotary shaker at 200 rpm. We did not use SFM because soya flour-containing SFM was less suitable than YS for both RNAseq experiments and acyl-CoA analysis (see below). Four different time points (48, 72, 96 and 120 h) were collected from wild type and *pirA*::pTYM-18 strains for each of the biological duplicates of the experiment. Total bacterial RNA was extracted from the pellets as described (Fondi et al., 2017). RNase-free DNase I was used to eliminate traces of DNA in the samples, in accordance with the instructions of the manufacturer (Promega, Madison, WI).

Ribosomal RNAs were depleted starting from 1 µg of total RNA from each of the time points and biological replicates by using the RiboZero Gram positive kit (Epicentre, Illumina), strand specific RNA-seq libraries were prepared by using the ScriptSeq™ v2 RNAseq library preparation kit (Epicentre, Illumina) starting from 50 ng of previously rRNA depleted RNA from each biological replicate and for all the time points analyzed. Then each library was sequenced on a MiSeq Illumina sequencer and 76 bp reads were produced.

2.5. RNAseq data analysis

Bowtie 2 (v2.2.6) (Langmead and Salzberg, 2012) was used to align raw reads to *S. ambofaciens* ATCC 23877 genome (GCF_001267885.1) as already described (Fondi et al., 2017)

rRNA depletion, strand specificity and gene coverage were evaluated using BEDTools (v2.24.0) (Quinlan and Hall, 2010) and SAMtools (v0.1.19) (Li et al., 2009) to verify the library preparation and sequencing performances as described (Pinatel and Peano, 2018). Raw read counts were obtained as described (Fondi et al., 2017), and R package DESeq2 (v1.14.1) (Love et al., 2014) was then used to normalize the counts.

Time course analysis was performed with MaSigPro (v 1.46.0) (Conesa et al., 2006; Nueda et al., 2014) with $\alpha=0.05$, $rsq=0.7$ to select the variables; 9 clusters of variable genes with similar trends of expression were obtained.

COG annotation was obtained through CDD database annotation (Marchler-Bauer et al., 2015). Raw data are publicly available at Sequence Reads Archive under accession numbers: PRJNA342588 for the wild type strain, and PRJNA430852 for *pirA::pTYM-18* strain.

2.6. Differential proteomic analysis

To perform 2D-DIGE analysis, total proteins were extracted from frozen biomass samples of triplicate cultivations of *S. ambofaciens* strains grown for 120 h in YS medium, at 28 °C, on a rotary shaker at 200 rpm. Protein extraction, labelling and two-dimensional electrophoretic separations were performed as previously reported (Gallo et al., 2010; 2016). To obtain digitalized 2D-DIGE images, Cy-Dye-labeled protein spots were revealed by using the Typhoon FLA 9500 laser scanner (GE Healthcare). To detect differentially represented protein species (*i.e.* protein spots showing more than 1.3-fold change in spot volume with $P \leq 0.05$ as statistically significant ANOVA value), image analysis was performed using the 2D-DIGE-enabled Image Master 2-D platinum version 7.0 (GE Healthcare, Sweden) (Gallo et al, 2016). Differentially represented spots were excised from silver-stained gels, and processed for protein identification as already reported (Palazzotto et al., 2016). They were excised, *in gel*-reduced with dithiothreitol, S-alkylated with

iodoacetamide, and digested with trypsin (Roche) (Scippa et al., 2010). Resulting digests were analyzed by nanoliquid chromatography (nanoLC)-electrospray (ESI)-linear ion trap (LIT)-tandem mass spectrometry (MS/MS) using a LTQ XL mass spectrometer (ThermoFisher, USA) equipped with a nano-spray source (ThermoFisher) coupled to an UltiMate 3000 RSLC chromatographer (ThermoFisher) (Moreno et al., 2011). Peptides digests were resolved on an Acclaim PepMap RSLC C18 column (150 × 0.075 mm) (ThermoFisher), which was eluted with 80% v/v aqueous acetonitrile containing 0.1% v/v formic acid in 0.1% v/v formic acid (Moreno et al., 2011). Raw MS and MS/MS data were searched by means of MASCOT search engine (version 2.2, Matrix Science, UK) against an updated NCBI non-redundant protein database (downloaded in December 2016). Database searches were carried out by using parameters already described (Moreno et al., 2011). In all cases, spectra visualization with manual verification of fragmentation attribution was preliminary to definitive assignment of protein candidates (Palazzotto et al., 2016).

2.7. Spiramycin production assay

Spiramycin production by *S. ambofaciens* broth cultures was assessed by high-performance liquid chromatography-electrospray ionization-mass spectrometry (HPLC-ESI-MS) as described (Calcagnile et al., 2018). At different time intervals, supernatants were filtered through Phenex-RC membrane (0.45 µm; Phenomenex). Five µl of a solution of erythromycin (1 mg/ml) (Sigma-Aldrich) in 30% v/v aqueous acetonitrile plus 210 µl of acetonitrile were added to 500 µl of filtrated samples; mixture samples were vortexed, centrifuged at 4 °C for 5 min, and then 2 µl of the supernatant were injected for spiramycin determination.

The high-performance liquid chromatography (HPLC)-ESI-MS apparatus consisted in a Surveyor MS quaternary pump coupled to a Finnigan LCQ Deca XP Plus mass spectrometer (ThermoFisher) equipped with an ESI source and a quadrupole ion trap analyzer. Xcalibur software (ThermoFisher) was used for instrument control and data analysis. The spectrometer was calibrated externally with a mixture of caffeine, MRFA and Ultramark (ThermoFisher) (De Benedetto and

Fanigliulo, 2009). The mass spectrometer operated in the positive-ion mode with the following settings: sheath gas, 60 units; auxiliary gas, 20 units; spray voltage, 1.5 kV; capillary temperature, 325 °C; capillary voltage, 10 V. Mass spectra were recorded in full scan MS in the m/z range 400-1100. Spiramycin I, II and III were resolved on a BioBasic C-18 analytical column (150 x 2.1 mm, particle size: 5 μm) (Thermo Scientific), which was eluted with 5 mM ammonium formate, pH 7.0 (solvent A) and LCMS-grade acetonitrile (solvent B), at a flow rate of 200 $\mu\text{l}/\text{min}$, applying the following gradient of solvent B: 0 min, 15%; 1 min, 15%; 15 min, 70%; 20 min, 70%; 21 min, 15%; 25 min, 15%. To minimize source fouling during analysis, the eluent was directed to the source only during erythromycin and spiramycin elution by using the divert valve on the mass spectrometer. Calibration curves were made based on peak area ratios of analyte/internal standards vs. analyte concentrations, using 6 points calibration standards in the range of 0.1 - 5.0 $\mu\text{g}/\text{ml}$ (0.1, 0.2, 0.5, 1.0, 2.5, and 5.0 $\mu\text{g}/\text{ml}$). The recoveries of the method, evaluated by spiking the samples with low (200 ng) and high (2 μg) levels of the analyte, were 97 and 93%, respectively.

The method limits of detection (LODs) and limits of quantification (LOQs) were determined using the samples fortified at the lower validation level. LODs and LOQs determined at S/N ratios of 3 and 10 for spiramycin were 20 and 67 ng/ml, respectively.

2.8. Antimycin production assay

Bacteria were cultivated in SFM broth. At different time points, 1 ml of cultivation broth was collected, lyophilized and then dissolved in 1 ml methanol. After centrifugation at 10,000 x g , the pellet was discarded and the supernatant was collected for the analysis. Antimycin was analyzed by HPLC using a System Gold programmable solvent module 125 (Beckman) equipped with a Nucleosil C8 analytical column (200 x 4.6 mm; particle size: 3 μm , pore dimension: 120 Å) (Macherey & Nagel) maintained at 25 °C, and a UV detector (350 nm). The column was eluted with water (solvent A) and methanol (solvent B), at a flow rate of 1 ml/min, applying the following

gradient of solvent B: 0 min, 10%, 20 min, 100%, 34 min, 100%, 44 min, 10%. Pure antimycin (Sigma Aldrich) was used as standard.

2.9. Survival to H₂O₂ exposure

S. ambofaciens spores were preliminarily subjected to a germination procedure, as described (Kieser et al., 2000). Briefly, a dense spore suspension (about 10¹⁰ spores/ml) was pelleted at 4000 rpm, for 10 min, and resuspended in 5 ml of 50 mM TES, pH 8. The suspension was heat shocked at 50 °C, for 10 min, cooled under cold tap, and finally added with an equal volume of double-strength Germination medium (1% yeast extract, 1% casamino acid, 10 mM CaCl₂) Then, the suspension was incubated at 37 °C, with shaking for 3 h. The germinated spores were pelleted and resuspended in water, with vigorous agitation to disperse the clumps. Five ml of YS broth were inoculated with germinated spores to OD₄₅₀ of 0.05, and incubated for 3 h, at 30 °C, under shaking. Finally, *S. ambofaciens* cultures were treated with different concentrations of H₂O₂, for 1 h, at 30 °C, before cells were harvested by centrifugation and plated on YS agar for the count.

2.10. Determination of intracellular short chain acyl-CoA pool

Samples of culture (50 ml) were collected by centrifugation at 10,000 x *g* for 10 min, at 4 °C. The mycelia were resuspended in 5 ml of 5 mM ammonium formate, pH 7.05, and then lysed by passing twice the suspension through a French Press operating at 1000 psi. Cell debris was removed by centrifugation at 10,000 x *g* for 20 min, at 4 °C, and the clarified cell lysate was lyophilized. Lyophilized extracts were dissolved in 500 µl of 10 mM ammonium formate, pH 4.6, containing [¹³C₃]-malonyl-CoA (2 µg/ml) as internal standard (I.S.), and filtered through a 0.2 µm membrane; 5 µl of each extract were analyzed by HPLC-ESI-MS/MS (Neubauer et al., 2015) with the same instrumentation used for the spiramycin production assay. Short-chain acyl-CoAs were resolved on a Accucore reversed phase column (100 x 2.1 mm, particle size: 2.6 µm) (Thermo Scientific), which was eluted with 10 mM formate pH 4.6/methanol 98/2 v/v (solvent A) and methanol (solvent

B), at a flow rate of 200 $\mu\text{l}/\text{min}$, applying the following gradient of solvent B: 0 min, 0%; 1 min, 0%; 10 min, 20%; 18 min, 70%; 25 min, 70%; 26 min, 0%.

Metabolite detection was performed in selected reaction monitoring mode (SRM), in five time windows, using the mass transitions reported in Table 1. CID was carried out on the parent ions using He as collision gas, with an isolation width of 2 m/z units and a MS^2 normalized collision energy of 35%. Standard solutions containing I.S. (2 $\mu\text{g}/\text{ml}$) with concentration values from 0.2 to 5 $\mu\text{g}/\text{ml}$ (0.2, 0.5, 1.25, 2.5 and 5.0 $\mu\text{g}/\text{ml}$) of each acyl-CoA were prepared by diluting corresponding stock solutions (1 mg/ml) in 10 mM ammonium formate, pH 4.6.

2.11. Determination of total lipid content by ATR-FTIR spectroscopy

Total lipid content was carried out by attenuated total reflectance - Fourier transform infrared (ATR-FTIR) spectroscopy (Deniset-Besseau et al., 2014) following the method described by Millan-Oropeza and colleagues (2017b). In particular, a Cary 600 FTIR spectrometer (Agilent Technologies) equipped with a DTGS detector and a diamond ZnSe ATR crystal (Pike MIRacle) was used. The spectra were recorded in the 4000 to 650 cm^{-1} ranges with a spectral resolution of 4 cm^{-1} ; in order to obtain good signal to noise ratio, 64 scans were added and averaged before Fourier transform. The background spectra were acquired before each sample measurement. Three measurements for each sample were made at different time points.

To evaluate the total esterified fatty acid content of the strains, a linear baseline correction was applied using Resolution Pro software and the intensity of the carbonyl stretching band at about 1740 cm^{-1} was considered for lipid determination; the intensity of the amide I peak at 1650 cm^{-1} was considered for evaluation of the protein content in the biomass samples. The CO/amide I ratio was used to monitor differences in triacylglycerols (TAG) accumulation between the different bacterial strains.

2.12. In silico modeling of protein structure and protein-protein interaction

Multiple sequence alignment and cluster analysis of acyl-CoA dehydrogenase (ACAD)-deduced amino acid sequences was carried out by ClustalW at Kyoto University Bioinformatic Center (<http://www.genome.jp/tools/clustalw/>). I-Tasser Suite (Yang et al., 2015) was used to generate 3D models of proteins from deduced amino acid sequences. Modeling is based on structure templates identified by LOMETS from the PDB library. The top 10 threading templates were selected according to Z-score, and the quality of models was assessed by C-Score. The meta-server Coach (I-Tasser Suite) was used to predict small ligands, protein ligands and the binding residues. The quality of the models was proved alternatively with Rampage (Lovell et al., 2003), which computes dihedral angles to value the quality of models and produce a corresponding Ramachandran Plot. We used these resources to screen 3D models and to select the best models for PirA (SAM23877_RS18305) and AcdB (SAM23877_RS18295). Homo-oligomerization was predicted by GalaxyGemini (Lee et al., 2013). To obtain a prevision on the formation of a molecular complex between PirA and AcdB, we submitted the models on docking software Gramm-X (Tovchigrechko and Vakser, 2006). This software is based on Lennard-Jones function to compute intermolecular potential energy (rigid body docking); FireDock (Mashiach et al., 2008) (flexible docking) was used to refine results generated by Gramm-X. We analyzed the results of docking by Find Clash/Contact (Mills and Dean, 1996) in order to obtain contact residues of AcdB in complex with PirA. PSiver (Murakami and Mizuguchi, 2010) predicted binding interfaces starting from amino acid sequences. The result was used as a filter to eliminate contact residues that fall in non-interface regions. To analyze functional domains of AcdB, we used Conserved Domain (Marchler-Bauer et al., 2015) that identifies active and catalytic residue based on sequence alignments. For 3D modeling, we also used Phyre2 (Kelley et al., 2015), which sent the top-ranking protein models to 3DLigandSite server (Wass et al., 2010) for binding sites prediction. Transmembrane region and topology predictions were carried out by TMMOD (Kahsay et al., 2005) and TMpred (Hofmann and Stoffel, 1993), respectively. DLP-SVM was used as a domain linker predictor (Ebina et al., 2009). ConSurf web server was used to estimate and visualize evolutionary conservation of amino acids to reveal

regions that are important for structure and/or function (Ashkenazy et al., 2016). The interaction of AcdB with acyl-CoA substrates was analyzed by SwissDock (Grosdidier et al., 2011). All results were processed by Chimera (Pettersen et al., 2004) and related tools. The contact residues between the two proteins (PirA and AcdB), the residues of AcdB ligands and the contact residues of AcdB in dimeric state are here shown by 3D images using different colors.

2.13. *In vitro protein-protein interaction*

The interaction between recombinant AcdB and PirA proteins was assayed *in vitro* by co-elution experiment using the affinity chromatography. *E. coli* BL21(DE3) competent cells were transformed with pET-AcdB-V5/His6 or pET-PirA-V5. Protein production was induced with IPTG, and cells were then lysed as described above. Clarified cell lysates (300 μ g) were mixed together, and incubated under rotation, at 4 °C, for 2 h. Then, the mix was bound to 1 ml of Ni-IMAC resin (Bio-Rad Laboratories) for 1 h, at 4 °C. The resulting slurry was transferred to a gravity-flow column, and washed twice with 1 ml of lysis buffer. The protein complex AcdB-V5/His6:PirA-V5 was then eluted with 50 μ l of elution buffer (20 mM Tris-HCl pH 8.0, 500 mM NaCl, 500 mM imidazole and 10% glycerol). Eluted proteins were fractionated by sodium dodecyl sulfate polyacrylamide gel electrophoresis (SDS-PAGE) and electrophoretically transferred onto a nitrocellulose membrane (BioTrace NT, Pall Life Science), according to standard procedures. To detect V5-tagged proteins, the membrane was incubated with the antibody against V5 epitope, for 1.5 h, at room temperature, and then with appropriate horseradish peroxidase-conjugated IgG, for 1 h. Signals were detected by enhanced chemiluminescence using the Amersham ECL plus kit (GE Healthcare, Milan, Italy).

2.14. *Determination of acyl-CoA dehydrogenase activity*

AcdB activity was assayed spectrophotometrically at 600 nm with phenazine methosulfate (PMS) as the primary electron acceptor and 2,6-dichlorophenolindophenol (DCPIP) as the final

electron acceptor (Lea et al., 2000). The assay mixture (100 μ l) contained 50 mM potassium phosphate (pH 7.6), 36 μ M DCPIP, 0.3 mM N-ethylmaleimide, 1.5 mM PMS, 100 ng purified recombinant AcdB. Upon equilibration at 30 °C for 5 min, 100 μ M palmitoyl-CoA was added to initiate the reaction. AcdB activity was measured spectrophotometrically by following the decrease in absorbance at 600 nm (ϵ DCPIP = 21 mM⁻¹ cm⁻¹). To evaluate the effect of AcdB:PirA interaction on AcdB activity, about 280 ng purified PirA (5-molar excess) was added in the reaction mixture. The oxidation of Fe(II)-PirA to Fe(III)-PirA was achieved by incubating purified PirA with 8 μ M potassium ferricyanide in a final volume of 5 μ l (potassium ferricyanide:PirA ratio = 5:1), for 15 min.

3. Results and Discussion

3.1. Phenotypes of *S. ambofaciens* ATCC 23877, *pirA*-defective and *pirA*-complemented strains

Phenotypic differences between wild type *S. ambofaciens* ATCC 23877 and derivative strain *pirA*::pTYM-18 were analyzed in different media. With respect to the wild type strain, the *pirA* mutant was characterized by an evident reduction of grey pigmentation of surface mycelium on SM-II agar (Fig. 1A). This phenotypic trait was assayed by spectral reflectance by using SM-II agar plates streaked to confluence and incubated at different time points (Fig. 1B and data not shown). This phenotypic difference between the strains was suggestive of some changes in secondary metabolism in *pirA*::pTYM-18.

This hypothesis was supported by results of microbiological assays that analyzed antibiotic production by *S. ambofaciens* strains growing on R2 agar using *Bacillus subtilis* as a tester microorganism (Supplementary Fig. 1). This bioassay was designed to detect the production of kinamycin in *S. ambofaciens* (Bunet et al., 2014). Results showed a time-dependent increase in antibiotic production in the wild type culminating at 120 h of growth (Supplementary Fig. 1). In contrast, antibiotic production was almost undetectable in *pirA*::pTYM18 (Supplementary Fig. 1).

Noticeably all these phenotypic traits could be genetically complemented by inserting an intact copy of *pirA* into vector plasmid pTYM-18 leading to strain *pirA*::pTYM-*pirA* (Fig. 1; Supplementary Fig. 1), although antibiotic production kinetics in R2 agar appeared to be different in *pirA*::pTYM-*pirA* and wild type. These results suggested that the phenotypic changes in *pirA*::pTYM-18 were due to *pirA* inactivation.

3.2. Spiramycin and antimycin production in *S. ambofaciens* ATCC 23877, *pirA*-defective and *pirA*-complemented strains

To analyze the modifications induced by *pirA* inactivation on secondary metabolism, we measured the production of spiramycin (Fig. 2) and antimycin (Supplementary Fig. 2). The analysis of the growth curves of wild type, *pirA*::pTYM-18 and complemented *pirA*::pTYM-*pirA* strains did not show any difference between strains in SFM broth (Fig. 2B). In YS broth final biomass values were slight lower (<10%) in both recombinant strains as compared to wild type (Fig. 2A). In this medium, the strains exhibited the typical two-stage growth curve of actinomycetes consisting of an initial stage of rapid growth (RG1), a transition phase (T), a secondary rapid growth phase (RG2) and a stationary (S) phase (Puglia et al., 1995). HPLC-ESI-MS data demonstrated that spiramycin production by *pirA*::pTYM-18 was severely reduced as compared to wild type in both YS and SFM broths (Fig. 2C, and Fig. 2D, respectively). Antibiotic production could be either partially (in YS) or almost fully (in SFM) restored to wild type levels by genetic complementation in *pirA*::pTYM-*pirA*. In SFM, antimycin production by *pirA*::pTYM-18 was also strongly reduced as compared to wild type strain; it was partially restored to wild type levels in complemented *pirA*::pTYM-*pirA* (Supplementary Fig. 2). These findings confirmed the inhibitory effects on polyketide biosynthesis caused by *pirA* inactivation.

3.3. Short chain acyl-CoA pools in *S. ambofaciens* ATCC 23877, *pirA*-defective and *pirA*-complemented strains

To establish whether reduced polyketide production as a result of *pirA* inactivation could be associated with reduced amounts of metabolic precursors, intracellular short-chain acyl-CoA pools were analyzed in the wild type, *pirA*::pTYM-18 and *pirA*::pTYM-*pirA* strains during the growth in YS broth. Four types of patterns were observed in *pirA*-defective strain with respect to both wild type and *pirA*::pTYM-*pirA* strains involving: i) the propionyl-CoA whose amounts were unchanged; ii) the malonyl-CoA whose levels increased; iii) the butyryl-CoA and crotonyl-CoA whose amounts decreased; iv) the acetyl-CoA, methylmalonyl-CoA and ethylmalonyl-CoA whose accumulation was shifted toward late growth stages (Fig. 3).

In particular, one most prominent effect of *pirA* inactivation was a large decrease of butyryl-CoA and crotonyl-CoA pools, and an increase of malonyl-CoA pool. In all strains, the butyryl-CoA pool reached the maximum concentration around 48 h. While in the wild type and *pirA*-complemented strains it attained the value of 109 and 69 $\mu\text{g/g}$ DCW, respectively, otherwise in *pirA*::pTYM-18 its maximum concentration was strongly reduced to about 10.9 $\mu\text{g/g}$ DCW. When compared to both wild type and *pirA*-complemented strains, the crotonyl-CoA pool was also dramatically decreased in *pirA*-defective strain. In contrast, the malonyl-CoA pool, which was detectable only at 24 h in both wild type and *pirA*::pTYM-*pirA*, possibly due to its rapid turnover, was greatly increased (about 26- and 9-fold, respectively) in *pirA*::pTYM-18.

Another striking effect of *pirA* inactivation was a different trend over time course of acetyl-CoA, methylmalonyl-CoA and ethyl-malonyl-CoA pools. In both wild type and *pirA*-complemented strains, the acetyl-CoA pool attained the maximum concentration at 24 h (about 196 and 212 $\mu\text{g/g}$ DCW, respectively), began to drop after this time point (to about 36 and 68 $\mu\text{g/g}$ DCW, respectively), and remained almost stable between 48 and 96 h. In *pirA*-defective strain, the acetyl-CoA pool exhibited a biphasic trend. When compared to other strains, it was lower at 24 h (about 78 $\mu\text{g/g}$ DCW) and substantially higher at 72 h (351 $\mu\text{g/g}$ DCW), before dropping at 96 h. Similar trends were observed when ethylmalonyl-CoA and methylmalonyl-CoA pools were analyzed, with few differences observed for the peak of methylmalonyl-CoA, which was attained at 48 h (instead

of 24 h as for acetyl-CoA and ethylmalonyl-CoA) in both wild type and *pirA*-complemented strains. The delay in the generation of acetyl-CoA and derived products such as methylmalonyl-CoA and ethylmalonyl-CoA (Erb et al., 2007; Jung et al., 2014; Zhang et al., 2010) might indicate a negative impact of *pirA* inactivation on either glycolysis or on fatty acid degradation (Fig. 4). The increase of the malonyl-CoA pool at early time points, in spite of the decreased acetyl-CoA pool, was also suggestive of an increased channeling of acetyl-CoA toward fatty acid biosynthesis by acetyl-CoA carboxylase (Fig. 4). In contrast, *pirA* inactivation seems to have no impact of propionyl-CoA metabolism.

The effects of *pirA* inactivation on short-chain acyl-CoA pools might well account for impaired synthesis of polyketide antibiotics in strain *pirA*::pTYM-18, with special reference to spiramycin. In fact, spiramycin macrolactone ring is built up by a PKS that, apart from the most common polyketide precursor malonyl-CoA and methylmalonyl-CoA, also incorporates the less common precursor ethylmalonyl-CoA, and the functionalized extender unit methoxymalonyl-CoA (Karray et al., 2007; Kuhstoss et al., 1996).

3.4. Time-resolved transcriptomics of *S. ambofaciens* ATCC 23877 and *pirA*-defective strain

Time course analysis identified 1604 genes with significantly different transcriptional profiles among the time points and between the two strains; they were classified into 9 clusters according to their gene expression profiles (Supplementary Table 1; Supplementary Fig. 3). 832 and 772 genes were more (Clusters **1, 5, 7, 8, 9**) and less (Clusters **2, 3, 4, 6**) expressed in the *pirA* mutant than in the wild type strain, respectively.

Genes more expressed in the *pirA* mutant than in the wild type strain were those involved in glycolysis (*pfkA*, *gpmA* and *pykF*), central carbon and energy metabolism and conversion (Fig. 4; Supplementary Table 1). These include genes coding for the E1 subunit of pyruvate dehydrogenase (*aceE*), as well as enzymes of the Krebs cycle (subunit E3 of pyruvate/2-oxoglutarate dehydrogenase [*lpd*], flavoprotein subunit [*sdhA*] and anchor subunit [*sdhD*] of succinate

dehydrogenase/fumarate reductase, Fe-S containing subunit of succinate dehydrogenase / fumarate reductase [*frdB*], beta subunit of succinly-CoA synthetase [*sucC*], fumarate hydratase [*fumB*]) and the malic enzyme (*sfcA*). Proteins of the respiratory chain, namely subunit 1 (*cyoB*) and 3 (*cyoC*) of cytochrome / quinol oxidase, and alpha (*atpA*), gamma (*atpG*), epsilon (*atpC*) and membrane subunits c (*atpE*) of F₀F₁ ATP synthase present in cluster **1** were also more expressed in the *pirA* mutant.

These data suggest that PirA has a negative impact on the expression of enzymes of the central carbon and energy metabolism. Consequently, the *pirA* mutant is characterized by an activation of central carbon metabolism resulting into an oxidative metabolism. The transcriptional up-regulation of *pstS*, *pstC*, *pstA* and *pstB* (encoding the phosphate transport system, cluster **8**) in the *pirA* mutant strain is consistent with the activation of the energy metabolism of this strain. An oxidative metabolism generates oxidative stress, and one notes the up-regulation of many genes involved in oxidative stress, including *katG* and *katE* (encoding catalases, cluster **8**), three *soxR* paralogs (cluster **5** and **7**), in addition to a number of genes involved in DNA recombination and repair (*uvrB*, *uvrD* in cluster **5**; *uvrC*, *recA*, *recD*, *recG*, *recO* and *xseA* in cluster **7**) that might indicate oxidative stress damage to DNA. Furthermore, experimental data demonstrated that *pirA*::pTYM-18 was much more sensitive than wild type strain to H₂O₂ exposure (Fig. 5).

The higher expression of some genes involved in amino acids (including *hisA*, *hisC*, *hisD*, *hisF*, *hisJ*, *pheA2*, *argD*, *aroG2*, *gdhA*, *glyA*, *lysA*, *ilvH*), and nucleotides (*purL1*, *purL2*, *hptA*, *pyrH*) biosynthesis (Fig. 4; Supplementary Table 1, cluster **1**, **5** or **7**) in the *pirA* mutant strain is also consistent with an activation of the Krebs cycle as well as with the lower expression of *spoT* (see below). Genes coding for transcription machinery (*rpoA*, *nusB*) and ribosomal proteins (*rplB*, *rplM*, *rpmF*, *rpmI*, *rpsF*, *rpsG*, *rpsM*) are also grouped within cluster **1**. Genes involved in DNA replication (*dnaX*, *gyrA*, *gyrB*), cell division and chromosome partitioning (*ftsI*, *ftsQ*, *ftsW*, *spo0J*) and cell wall biosynthesis (*murE*, *rfe*) also belonged to cluster **7**. Noteworthy, genes involved in the biosynthesis of fatty acids (*fabB*, *fabH*; other *fabH* paralogs), phosphatidylglycerol (*plsC*) and

cardiolipin (*cls*, *pgsA*, *cdsA*, *plsC*), isoprenoid lipids through the methylerythritol phosphate pathway (*ispA*, *ispG*, *uppS*) as well as genes involved in the beta-oxidation of fatty acids (*acdA*, *acdB*) and *fadB* were clearly up-regulated in *pirA* mutant (cluster **1**, **5**, **7**, **8** or **9**).

In the *pirA* mutant, one also notes the transcriptional up-regulation of genes belonging to cluster **7** involved in the generation of building blocks for polyketide antibiotics (i.e. malonyl-CoA, methylmalonyl-CoA and ethylmalonyl-CoA). These include genes encoding methylmalonyl-CoA carboxyltransferase (*mct*), methylmalonyl-CoA mutase (*sbm*) and L-malyl-CoA/beta-methylmalyl-CoA lyase (*mclA*). *mcd*, *mclA* and *msd* code for enzymes involved in ethylmalonyl-CoA metabolism, whose importance in spiramycin production was already demonstrated (Fondi et al., 2017). However, although the production of spiramycin is centered at 50 h, metabolites of the ethylmalonyl-CoA pathway were rather detected around 80 h. Other enzymes such as mesaconyl-CoA hydratase (*mcd*, cluster **1**), acetyl-CoA/propionyl-CoA carboxylase alpha subunit (*accA/pccA*, cluster **5**), and methylsuccinyl-CoA dehydrogenase (*msd*, cluster **9**) were also more expressed in the *pirA* mutant but to a lesser extent.

Conversely, clusters **2**, **3**, **4**, and **6** exhibited lower expression levels in *pirA* mutant compared to wild type strain. One notes the presence in cluster **2** of *spoT*, encoding the enzyme involved in the biosynthesis of (p)ppGpp. (p)ppGpp is a major modulator of bacterial growth and general metabolism. It negatively controls the expression of genes involved in rRNA, amino acid and nucleotide biosynthesis (Hauryliuk et al., 2015). It is also a global regulator of morphological and biochemical differentiation in streptomycetes (Hesketh et al., 2007; Ochi, 1987). Interestingly, genes coding for ribosomal proteins (*rpsT*, *rpmA*, cluster **6**), EF-Tu and EF-G (*tufB* and *fusA*, cluster **3**), and translation elongation factor P (*efp*, cluster **6**), as well as genes involved in the modifications of rRNA, tRNA, and ribosomal proteins (*trmA*, *rimK*, *rimL*, cluster **2** or **6**; *spoU*, cluster **4**) and aminoacyl-tRNA synthetases (*serS*, *proS*, *tsaB*, cluster **2**) were also down-regulated in the *pirA* mutant. Clusters **2** and **4** also contain genes involved in glycine, serine and threonine (*serB*, *glyA*, *thrC*) and purine (*purB*) metabolism as well as *aceF*, which codes for E2 subunit of the

pyruvate/2-oxoglutarate dehydrogenase complex, whereas up-regulation of E1 and E3 subunits was observed in the *pirA* mutant. Noteworthy, one of the two paralogous genes coding for triacylglycerol esterase/lipase (*estA*) was down-regulated in *pirA* mutant (cluster 4), while the other was more expressed in *pirA* mutant but to a lesser extent (cluster 9).

Cluster 3 includes genes involved in the utilization of complex carbon sources like starch and glycogen (including *gdb1*), genes encoding acyl-CoA dehydrogenases as well as *gapA* encoding glyceraldehyde-3-phosphate dehydrogenase. This enzyme is inhibited by H₂O₂-induced ROS in streptomycetes (Wei et al., 2011). The down-regulation of the glyceraldehyde-3-phosphate dehydrogenase in the *pirA* mutant might lead to accumulation of glycerol-3-phosphate, a necessary precursor of TAG biosynthesis, whereas the down-regulation of several acyl-CoA dehydrogenases and TAG esterase/lipase might slow down TAG / fatty acid degradation. Other relevant genes mapping in this cluster play a role in cell division (*ftsI*, *ftsW*), cell shape determination and cytoskeleton assembly (*mreB*, *mreC*), and cell wall remodeling including D-alanine-D-alanine carboxypeptidase (*dacC*), lysozyme M1 (*acm*) and murein DD-endopeptidase (*nlpD*), although other *ftsI*, *ftsW*, *dacC*, *acm* and *nlpD* paralogs showed an opposite trend of regulation. Cluster 6 contains genes encoding subunits of carbon monoxide dehydrogenase (*coxL*, *coxM*) and, importantly, several genes of the spiramycin biosynthetic gene cluster involved in sugar decoration of the macrolactone backbone, and methoxymalonate precursor biosynthesis.

Above-mentioned findings were corroborated by proteomic comparison of *S. ambofaciens* ATCC 23877 and *pirA::pTYM-18* biomass samples collected during stationary phase (*i.e.* 120 h of incubation) (Supplementary Fig. 4; Supplementary Table 2; Supplementary Table 3). At this time point, production profiles of biomass and antibiotic spiramycin stabilized. Indeed, the abundance pattern of differentially represented proteins and corresponding functional families inferred from KEGG database (Kanehisa et al., 2014) confirmed a role of *pirA* in controlling: i) translational events (*e.g.* down- and over-representation of RpsO and ClpC in the *pirA*-defective strain, respectively); ii) carbon metabolism (*e.g.* down-representation of GapA, PyrK and Lpd in the *pirA*-

defective strain); iii) spiramycin biosynthesis (*e.g.* down-representation of Srm25C in the *pirA*-defective strain); iv) oxidative stress response (*e.g.* down-representation of an alkylhydroperoxidase, KatE and SodF in the *pirA*-defective strain).

3.5. Total lipid content in *S. ambofaciens* ATCC 23877, *pirA*-defective and *pirA*-complemented strains

The metabolic effects of *pirA* inactivation might be explained hypothesizing a PirA-dependent modulation of fatty acid metabolism. To address this hypothesis, total lipid content was determined in the three strains by ATR-FTIR spectroscopy (Fig. 2E; Supplementary Fig. 5). In these experiments, bacteria were grown in YS broth, and harvested at different time points. Results demonstrated differences between the strains. In particular, they showed an evident increase of the ratio between the maximum absorption of the C=O ester stretching band of ester carbonyls and the maximum absorption of amide I band of proteins (CO/amide I) at later time points (96-168 h) (Fig. 2E). In particular, at 120 h the CO/amide I ratio in *pirA*::pTYM-18 was about three-fold higher than in the two other strains, suggesting a substantial increase in the ratio between total lipid esters (neutral TAG and polar membrane lipids) and proteins, as a consequence of *pirA* inactivation.

The effect of *pirA* inactivation on total lipid esters contents is noteworthy in light of the tight interplay between spiramycin production and lipid metabolism, which was previously proposed (Schauner et al., 1999). The existence of such an intimate connection between synthesis of fatty acids and production of polyketide antibiotics is becoming increasingly evident also in other streptomycetes (Le Maréchal et al., 2013). For example, Craney and colleagues (2012) demonstrated that the yields of polyketides, including actinorhodin, doxorubicin, baumycin and germicidin, can be significantly increased by sub-inhibitory concentrations of tricolosan, a known inhibitor of the FabI enoyl reductase. This finding suggests the existence of a balance between fatty acid and polyketide biosynthesis in the cell, which regulates polyketide yields (Craney et al. 2012). More recently, a link between polyketide production, TAG storages and beta-oxidation was proven

by analyzing actinorhodin (ACT) production in *S. coelicolor* A3(2) and *S. lividans*, two model streptomycetes that have identical pathways for lipid and secondary metabolite biosynthesis, but show very different abilities to produce antibiotics and accumulate TAG storages (Esnault et al., 2017). *S. lividans*, a weak producer of ACT, had high TAG content indicative of glycolytic metabolism, while *S. coelicolor* A3(2), a strong producer of ACT, was characterized by low TAG content, active consumption of polyphosphate storages and extremely high ATP/ADP ratios (Esnault et al., 2017). Proteomics helped to elucidate the different physiology of these closely related streptomycetes, confirming that oxidative metabolism predominates in *S. coelicolor* versus glycolytic metabolism in *S. lividans* (Millan-Oropeza et al., 2017a). Similar to *S. lividans*, the *pirA*-defective strain was characterized by a low polyketide production and a high intracellular lipid ester content.

The pleiotropic phenotype of the *pirA* mutant seems to be correlated with complex effects on the expression of various enzymes of central carbon and energy metabolism that might result in an oxidative metabolism that is known to generate oxidative stress. Consistently, an increased sensitivity to oxidative stress and the induction of various enzymes involved in the resistance to oxidative stress suggest that the *pirA* mutant suffers higher oxidative stress than the wild type strain. A high oxidative stress is usually linked to an active oxidative metabolism that generates a quantity of reduced co-factors exceeding the regeneration capacity of the respiratory chain. This leads to electrons leakage toward secondary acceptors and thus generates oxidative stress (Imlay 2009; 2013).

One way to reduce oxidative stress might be to down-regulate expression of enzymes of central carbon metabolism and, more especially, of the Krebs cycle that generate reduced cofactors. One notes that the expression of such enzymes is enhanced in the *pirA* mutant strain suggesting that PirA down regulates the expression of these enzymes. Another way to reduce Krebs cycle activity is to reduce acetyl-CoA availability either by inhibiting glycolysis or lipid degradation. Indeed, data

suggest that *pfkA*, *gpmA* and *pykF* as well as *aceE*, *lpd*, *acdB*, *fabB* and *fadA* expression might also be negatively regulated by PirA since their expression is high in the *pirA* mutant.

The low acetyl-CoA concentration in the *pirA* mutant before 48 h is correlated with an important peak of malonyl-CoA at 24 h, suggesting that the acetyl-CoA carboxylase is negatively regulated by PirA, and thus highly expressed in the *pirA* mutant. The relief of this negative regulation in the *pirA* mutant might drain most acetyl-CoA available toward malonyl-CoA synthesis, impairing the synthesis of other precursors used for the biosynthesis of spiramycin.

The late high acetyl-CoA availability (centered on 72 h) is correlated with enhanced ethylmalonyl-CoA (synthesized from two acetyl-CoA) and methylmalonyl-CoA availability. These two molecules could be considered as belonging to the same biosynthetic pathway (Fig. 4). The disappearing of this peak might indicate the storing of acetyl-CoA as TAG (around 120 h, Fig. 2E) that are remobilized afterwards. In brief, before 48 h most acetyl-CoA seems to be directed toward the synthesis of malonyl-CoA, then acetyl-CoA would be metabolized through the ethylmalonyl-CoA route, and at last acetyl-CoA is stored as TAG.

3.6. In silico modeling of the interaction between PirA and very long-chain acyl-CoA dehydrogenase *AcdB*

As already mentioned, there is evidence of physical and functional interaction between bacterial pirins and dehydrogenases (Lauchnor et al., 2011; Chan et al., 2009). This finding prompted us to investigate a possible interaction between PirA and acyl-CoA dehydrogenases (ACADs). ACADs constitute a rather large family of flavoproteins with nine known members (Ghisla and Thorpe, 2004; Kim and Miura, 2004). Members of the ACAD family are involved in fatty acid beta-oxidation catalyzing the first step of the beta-oxidation cycle. Based on their substrate chain length specificity and some structural features, the ACADs involved in fatty acid beta-oxidation are classified into: short-chain ACADs (SCADs) medium-chain ACADs (MCADs), long-chain ACADs (LCADs), and very long-chain ACADs (vLCADs) (Ghisla and Thorpe, 2004; Kim and Miura,

2004). With the exception of vLCADs, all these proteins are soluble homo-tetramers having a subunit mass of approximately 40 kDa, and each subunit contains a single FAD molecule. vLCADs form homo-dimers with a subunit mass of approximately 70 kDa, with one FAD molecule per monomer; they are membrane-associated by means of transmembrane regions.

Two dozen of ACAD-encoding genes were annotated in the genome sequence of *S. ambofaciens* ATCC 23877. Cluster analysis of deduced amino acid sequences of ACAD-encoding genes, and inspection of functional domains by Conserved Domain Database (Marchler-Bauer et al., 2015) allowed us to predict substrate specificity for most of them (Supplementary Fig. 6A). With reference to transcriptomic data, we noticed that two SCAD-encoding genes, namely SAM23877_RS06845 and SAM23877_RS13250 (*acdA*), together with two vLCAD-encoding genes, namely SAM23877_RS25730 and SAM23877_RS18295 (*acdB*), were more expressed in the *pirA*-defective strain (Fig. 4; Supplementary Table 1). Interestingly, *acdB* (SAM23877_RS18295) mapped very close to *pirA* (SAM23877_RS18305) (Supplementary Fig. 7A).

Preliminarily, the possible physical interaction between the vLCAD encoded by *acdB* and PirA was investigated by means of *in silico* modeling (Fig. 6). AcdB exhibits the same structural organization of a (v)LCAD from *Acinetobacter* sp. strain M-1, with a transmembrane domain at the carboxyl-terminal region (Tani et al., 2002) (Supplementary Fig. 6B). This enzyme was active toward longer acyl-CoA substrates with C₁₂ as optimum, a range of C₆-C₂₀ and almost negligible activity towards C₄ (Tani et al., 2002).

Five models of PirA and two models of AcdB were generated by I-Tasser Suite (Yang et al., 2015), and validated with Ramachandran plot by Rampage. The best models of both proteins were then selected (Fig. 6A), and used for further analyses. The C-Scores (min -5 max 2) of selected models were 0.06 and 0.22 for AcdB and PirA, respectively. Results of Rampage demonstrated good quality of selected models. Indeed, the dihedral angles were 79.9% (AcdB) and 82.4% (PirA) in favored regions, 12.8% (AcdB) and 10.8% (PirA) in allowed regions, while the rest of residues fell in outlier regions. Similar to hPirin (Pang et al., 2004), *S. ambofaciens* PirA was predicted to be

characterized by two β -barrel domains, with a Fe(III)/Fe(II) cofactor bound within the cavity of the N-terminal domain. In addition, a α -helix domain was predicted in the C-terminal region (Fig. 6A, left). AcdB exhibited the typical structure of vLCAD consisting of an N-terminal α -helical domain, a central region including a β -sheet domain and an α -helical domain common to all ACADs, and a C-terminal α -helical bundle absent in other ACADs and perpendicular to the N-terminal α -helical domain (Fig. 6A, right; Fig. 6B). Similar to all vLCADs, Galaxy-GeminiWEB predicted that AcdB was active in a dimeric state. Each monomer was predicted by SwissDock to bind FAD as cofactor, and to accommodate 6-22 carbon acyl-CoAs as optimal substrates (Fig. 6C).

The PirA and AcdB models were used as input for *in silico* docking by Gramm-X (rigid body docking based on Lennard-Jones function) and FireDock web tools (flexible docking, to refine Gramm-X results) to look at possible interactions. Free binding energy computed by Gramm-X and FireDock was -70.34 KJ/mol. By examining the predicted complexes, *i.e.*, AcdB/Ac dB dimer (Fig. 6A, right) vs. AcdB/PirA with Chimera (Find Clashes/Contact), it was possible to identify a binding interface and the most important residues for complex formation (Fig. 6D, left and right). To refine the analysis, the putative contact residues of AcdB were filtered by means of PSiver, which predicts physically interacting residues using a Naïve Bayes classifier method based on sequence features. To visualize the possible effects of the AcdB/PirA interaction, all residues detected (including those involved in acyl-CoA substrate binding, FAD cofactor binding, AcdB homo-dimerization, and interaction with PirA) were reported in a 3D image showing the AcdB/PirA complex (Fig. 6E). Most of AcdB residues involved in the interaction with PirA lie within the C-terminal α -helical bundle (Fig. 6B) and in the contact interface between AcdB monomers (Fig. 6E).

3.7. Overexpression and purification of tagged PirA and AcdB, interaction and enzymatic assay

The putative interaction between PirA and AcdB was evaluated *in vitro* by co-elution experiments. The *E. coli* cell lysates containing overexpressed V5-His6-tagged AcdB (AcdB-

V5/His6) and V5-tagged PirA (PirA-V5) (Supplementary Fig. 8) were prepared and tested by Western blot analysis using an antibody against V5 epitope (Fig. 7A, lanes 1 and 2). The *E. coli* cell lysates were used singularly or in a mix in the affinity chromatography. As expected, Western blot analysis showed that AcdB-V5/His6 was retained and then eluted by the IMAC resins when the corresponding *E. coli* cell lysate was applied in the affinity chromatography (Fig. 7A, lanes 3 and 4). A band corresponding to the expected PirA-V5 dimension was observed upon chromatography analysis carried out with the mix of PirA-V5 and AcdB-V5/His6 enriched cell lysates (Fig. 7A, lanes 3), but not with the PirA-V5 enriched cell lysate alone (Fig. 7A, lanes 5).

The effect of the PirA:AcdB interaction on AcdB enzymatic activity was then analyzed by using His6-tagged AcdB (AcdB-His6) and PirA (PirA-His6). The results demonstrated an enzymatic activity of 1.43 ± 0.12 U/mg with palmitoyl-CoA as AcdB-His6 substrate (Fig. 7B). The activity slightly decreased to about 63% (0.90 ± 0.15 U/mg) when a 5-fold molar excess of purified PirA-His6 was added in the reaction mix. The influence of the redox state of Fe-PirA was then evaluated. To this purpose, purified PirA-His6 was pre-incubated with a 5-molar excess of potassium ferricyanide, converting Fe(II)-PirA-His6 into Fe(III)-PirA-His6. A remarkable inhibition of AcdB to less than 10% of the initial enzymatic activity (0.14 ± 0.08 U/mg) was observed upon addition of Fe(III)-PirA in the reaction mix (Fig. 7B).

Altogether, these findings are consistent with a model in which PirA modulates fatty acid beta-oxidation in response to redox state. Pirins are non-heme iron-binding proteins with the iron located in an open cleft near an R-shaped loop (Fig. 6A). In human cells, hPirin binds and activates NF- κ B in a redox-dependent manner. hPirin-Fe(III) is the active form, while hPirin-Fe(II) is the resting form (Liu et al., 2013). Moreover, a recent study demonstrates that the restricted conformational space and electrostatic complementary of hPirin-Fe(III) are crucial for binding and regulation of NF- κ B (Barman and Hamelberg, 2016). Consistently with this model, here we show that the oxidized form of PirA strongly inhibited AcdB activity *in vitro* (Fig. 7B). Since ROS are known to

be able to oxidize Fe(II) to Fe(III), it is reasonable to assume that PirA acts as a redox sensor modulating fatty acid beta-oxidation as a function of ROS levels.

Deregulated vLCAD activity may trigger oxidative stress in *pirA* mutant. In fact, there is evidence that high beta-oxidation levels may induce oxidative stress in bacteria. For instance, high intracellular H₂O₂ levels are generated by growth of *Escherichia coli* on fatty acids as result of endogenous H₂O₂ generation by auto-oxidation of FADH₂ produced during the beta-oxidation (Doi et al., 2014). In addition, vLCAD can transfer electrons to ETF, which then reduces ETF-quinone oxidoreductase (ETF-QQ) with the possibility of electron leakage from both sites and reactive oxygen species (ROS) generation, depending on the electron transport chain (ETC) redox state (Seifert et al., 2010).

The important role of Pirin as modulator of fatty acid metabolism and oxidative stress levels is further supported by physical location of the *pirA* paralogs, namely *pirA2* (SAM23877_RS11555) and *pirA4* (SAM23877_RS05960), in close proximity to a fatty acid biosynthetic gene cluster (*fabD-fabH-acpP-fabB*) (SAM23877_RS11565-SAM23877_RS11580) and to a gene encoding an alkylhydroperoxidase/carboxymuconolactone decarboxylase family protein (SAM23877_RS05965), respectively. On the other hand, the fourth paralog *pirA3* is adjacent to congocidine biosynthetic gene cluster (Supplementary Fig. 7A). Supplementary Fig. 7B shows that average expression values of *pirA* increased as a function of time in the wild type strain, thus suggesting an important role of PirA during late growth and mostly during stationary phases, when bacteria are more exposed to oxidative injury.

4. Conclusions

In all living cells, the accurate balance between beta-oxidation and fatty acid synthesis prevents futile cycling between them (Fujita et al., 2007; Schujman and de Mendoza, 2008). Here we provide the evidence that PirA (SAM23877_RS18305) is a novel redox-sensitive negative modulator of the activity of vLCAD (AcdB), which catalyzes the first committed step of the beta-oxidation cycle.

pirA inactivation resulted in many phenotypic changes, depressed polyketide antibiotic production, and wide metabolic perturbations that were reflected by transcriptional changes mostly affecting genes involved in central carbon and lipid metabolism. These changes underlie a modified carbon flow between glycolysis, Krebs cycle, ethylmalonyl-CoA pathway, and lipid metabolism, with an increased and deregulated flow through the beta-oxidation and compensatory lipid biosynthesis at early growth stages, and accumulation of lipid esters at later time points. Indeed, dramatic modifications in the intracellular concentration and distribution over the time course of short chain acyl-CoA pools were observed in the *pirA*-defective strain, as compared to wild type and *pirA*-complemented strains. These changes may well account for decreased spiramycin production, since a balanced and timely feeding of these precursor monomers is a prerequisite for effective spiramycin biosynthesis. Altogether these findings confirm the existence of an intimate connection between lipid metabolism and polyketide antibiotic biosynthesis, and identify PirA as a key factor in the regulation of central carbon and lipid metabolism.

Acknowledgements

2D-DIGE analysis was performed using the instruments of Advanced Technologies Network (ATeN) Center at the University of Palermo, acquired in the frame of "Mediterranean Center for Human Health Advanced Biotechnologies" (Med-CHHAB) project (Project code: PONA3_00273 – Avviso MIUR D.D. n. 254/Ric del 18/05/2011). This work was partially supported by the Italian Ministry for Education, Universities and Research [Grant number PON01_02093 to PA].

References

- Adams, M.A., Jia, Z., 2005. Structural and biochemical evidence for an enzymatic quinone redox cycle in *Escherichia coli*: identification of a novel quinol monooxygenase. *J. Biol. Chem.* 280, 8358–8363.
- Ashkenazy, H., Abadi, S., Martz, E., Chay, O., Mayrose, I., Pupko, T., Ben-Tal, N., 2016. ConSurf 2016: an improved methodology to estimate and visualize evolutionary conservation in macromolecules. *Nucleic Acids Res.* 44, W344-W350.
- Baltz, R.H., 2012. Streptomyces temperate bacteriophage integration systems for stable genetic engineering of actinomycetes (and other organisms). *J. Ind. Microbiol. Biotechnol.* 39, 661-672.
- Barman, A., Hamelberg, D., 2016. Fe(II)/Fe(III) redox process can significantly modulate the conformational dynamics and electrostatics of Pirin in NF- κ B Regulation. *ACS Omega* 1, 837–842.
- Bentley, S.D., Chater, K.F., Cerdeño-Tárraga, A.M., Challis, G.L., Thomson, N.R., James, K.D., Harris, D.E., Quail, M.A., Kieser, H., Harper, D., Bateman, A., Brown, S., Chandra, G., Chen, C.W., Collins, M., Cronin, A., Fraser, A., Goble, A., Hidalgo, J., Hornsby, T., Howarth, S., Huang, C.H., Kieser, T., Larke, L., Murphy, L., Oliver, K., O’Neil, S., Rabbinowitsch, E., Rajandream, M.A., Rutherford, K., Rutter, S., Seeger, K., Saunders, D., Sharp, S., Squares, R., Squares, S., Taylor, K., Warren, T., Wietzorrek, A., Woodward, J., Barrell, B.G., Parkhill, J., Hopwood, D.A., 2002. Complete genome sequence of the model actinomycete *Streptomyces coelicolor* A3(2). *Nature* 417, 141–147.
- Bunet, R., Riclea, R., Laureti, L., Hôtel, L., Paris, C., Girardet, J.M., Spitteller, D., Dickschat, J.S., Leblond, P., Aigle, B., 2014. A single Sfp-type phosphopantetheinyl transferase plays a major role in the biosynthesis of PKS and NRPS derived metabolites in *Streptomyces ambofaciens* ATCC23877. *PLoS One* 9, e87607.
- Calcagnile, M., Bettini, S., Damiano, F., Talà, A., Tredici, S.M., Pagano, R., Di Salvo, M., Siculella, L., Fico, D., De Benedetto, G.E., Valli, L., Alifano, P., 2018. Stimulatory effects of

- methyl- β -cyclodextrin on spiramycin production, and physical chemical characterization of nonhost@guest complexes. *ACS Omega* 3, 2470-2478.
- Calos, M.P. 2006., The \square C31 integrase system for gene therapy. *Curr Gene Ther* 6, 633–645.
- Chan, Y.A., Podevels, A.M., Kevany, B.M., Thomas, M.G., 2009. Biosynthesis of polyketide synthase extender units. *Nat. Prod. Rep.* 26, 90-114.
- Conesa, A., Nueda, M.J., Ferrer, A., Talón, M., 2006. maSigPro: a method to identify significantly differential expression profiles in time-course microarray experiments. *Bioinformatics* 22, 1096–1102.
- Craney, A., Ozimok, C., Pimentel-Elardo, S.M., Capretta, A., Nodwell, J.R., 2012. Chemical perturbation of secondary metabolism demonstrates important links to primary metabolism. *Chem. Biol.* 19, 1020-1027.
- D'Argenio, V., Petrillo, M., Pasanisi, D., Pagliarulo, C., Colicchio, R., Talà, A., de Biase, M.S., Zanfardino, M., Scolamiero, E., Pagliuca, C., Gaballo, A., Cicatiello, A.G., Cantiello, P., Postiglione, I., Naso, B., Boccia, A., Durante, M., Cozzuto, L., Salvatore, P., Paoletta, G., Salvatore, F., Alifano, P., 2016. The complete 12 Mb genome and transcriptome of *Nonomuraea gerenzanensis* with new insights into its duplicated "magic" RNA polymerase. *Sci. Rep.* 6, 18.
- De Benedetto, G.E., Fanigliulo, M., 2009. A new CE-ESI-MS method for the detection of stable hemoglobin acetaldehyde adducts, potential biomarkers of alcohol abuse. *Electrophoresis* 30, 1798-1807.
- Dechend, R., Hirano, F., Lehmann, K., Heissmeyer, V., Ansieau, S., Wulczyn, F.G., Scheidereit, C., Leutz, A., 1999. The Bcl-3 oncoprotein acts as a bridging factor between NF-kappaB/Rel and nuclear co-regulators. *Oncogene* 18, 3316–3323.
- Deniset-Besseau, A., Prater, C.B., Virolle, M.J., Dazzi, A., 2014. Monitoring TriAcylGlycerols accumulation by Atomic Force Microscopy Based Infrared Spectroscopy in *Streptomyces* species for biodiesel applications. *J. Phys. Chem. Lett.* 5, 654–658.

- Doi, H., Hoshino, Y., Nakase, K., Usuda, Y., 2014. Reduction of hydrogen peroxide stress derived from fatty acid beta-oxidation improves fatty acid utilization in *Escherichia coli*. *Appl. Microbiol. Biotechnol.* 98, 629-639.
- Ebina, T., Toh, H., Kuroda, Y., 2009. Loop-length-dependent SVM prediction of domain linkers for high-throughput structural proteomics. *Biopolymers* 92, 1-8.
- Erb, T.J., Berg, I.A., Brecht, V., Muller, M., Fuchs, G., Alber, B.E., 2007. Synthesis of C5-dicarboxylic acids from C2-units involving crotonyl-CoA carboxylase/reductase: the ethylmalonyl-CoA pathway. *Proc. Natl. Acad. Sci. U.S.A.* 104, 10631-10636.
- Esnault, C., Dulermo, T., Smirnov, A., Askora, A., David, M., Deniset-Besseau, A., Holland, I.B., Virolle, M.J., 2017. Strong antibiotic production is correlated with highly active oxidative metabolism in *Streptomyces coelicolor* M145. *Sci. Rep.* 7, 200.
- Fondi, M., Pinatel, E., Talà, A., Damiano, F., Consolandi, C., Mattorre, B., Fico, D., Testini, M., De Benedetto, G.E., Siculella, L., De Bellis, G., Alifano, P., Peano, C., 2017. Time-resolved transcriptomics and constraint-based modeling identify system-level metabolic features and overexpression targets to increase spiramycin production in *Streptomyces ambofaciens*. *Front. Microbiol.* 8, 835.
- Fujita, Y., Matsuoka, H., Hirooka, K., 2007. Regulation of fatty acid metabolism in bacteria. *Mol. Microbiol.* 66, 829-839.
- Gallo, G., Alduina, R., Renzone, G., Thykaer, J., Bianco, L., Eliasson-Lantz, A., Scaloni, A., Puglia, A.M., 2010. Differential proteomic analysis highlights metabolic strategies associated with balhimycin production in *Amycolatopsis balhimycina* chemostat cultivations. *Microb. Cell Fact.* 9, 95.
- Gallo, G., Renzone, G., Palazzotto, E., Monciardini, P., Arena, S., Faddetta, T., Giardina, A., Alduina, R., Weber, T., Sangiorgi, F., Russo, A., Spinelli, G., Sosio, M., Scaloni, A., Puglia, A.M., 2016. Elucidating the molecular physiology of lantibiotic NAI-107 production in *Microbispora* ATCC-PTA-5024. *BMC Genomics* 17, 42.

- Ghisla, S., Thorpe, C., 2004. Acyl-CoA dehydrogenases. A mechanistic overview. *Eur. J. Biochem.* 271, 494-508.
- Grosdidier, A., Zoete, V., Michielin, O., 2011. SwissDock, a protein-small molecule docking web service based on EADock DSS. *Nucleic Acids Res.* 39, W270-W277.
- Hauryliuk, V., Atkinson, G.C., Murakami, K.S., Tenson, T., Gerdes, K., 2015. Recent functional insights into the role of (p)ppGpp in bacterial physiology. *Nat. Rev. Microbiol.* 13, 298-309.
- Hesketh, A., Chen, W.J., Ryding, J., Chang, S., Bibb, M., 2007. The global role of ppGpp synthesis in morphological differentiation and antibiotic production in *Streptomyces coelicolor* A3(2). *Genome Biol.* 8, R161.
- Hihara, Y., Muramatsu, M., Nakamura, K., Sonoike, K., 2004. A cyanobacterial gene encoding an ortholog of Pirin is induced under stress conditions. *FEBS Lett.* 574, 101–105.
- Hofmann, K., Stoffel, W., 1993. TMbase - A database of membrane spanning proteins segments. *Biol. Chem. Hoppe Seyler* 374, 166.
- Ikeda, H., Ishikawas, J., Hanamoto, A., Shinose, M., Kikuchi, H., Shiba, T., Sakaki, Y., Hattori, M., Omura, S., 2003. Complete genome sequence of and comparative analysis of the industrial microorganism *Streptomyces avermitilis*. *Nat. Biotechnol.* 21, 526–531.
- Imlay, J.A., 2009. Oxidative stress, in: Böck A, Curtis R III, Kaper J, Karp PD, Neidhardt FC, Nystrom T, et al. (Eds), *EcoSal-Escherichia coli and Salmonella: Cellular and Molecular Biology*. ASM Press, Washington, DC.
- Imlay, J.A., 2013. The molecular mechanisms and physiological consequences of oxidative stress: lessons from a model bacterium. *Nat. Rev. Microbiol.* 11, 443-454.
- Jung, W.S., Kim, E., Yoo, Y.J., Ban, Y.H., Kim, E.J., Yoon, Y.J., 2014. Characterization and engineering of the ethylmalonyl-CoA pathway towards the improved heterologous production of polyketides in *Streptomyces venezuelae*. *Appl. Microbiol. Biotechnol.* 98, 3701-3713.

- Kahsay, R.Y., Gao, G., Liao, L., 2005. An improved hidden Markov model for transmembrane protein detection and topology prediction and its applications to complete genomes. *Bioinformatics* 21, 1853-1858.
- Kanehisa, M., Goto, S., Sato, Y., Kawashima, M., Furumichi, M., Tanabe, M., 2014. Data, information, knowledge and principle: back to metabolism in KEGG. *Nucleic Acids Res.* 42, D199-D205.
- Karray, F., Darbon, E., Oestreicher, N., Dominguez, H., Tuphile, K., Gagnat, J., Blondelet-Rouault, M.H., Gerbaud, C., Pernodet, J.L., 2007. Organization of the biosynthetic gene cluster for the macrolide antibiotic spiramycin in *Streptomyces ambofaciens*. *Microbiology* 153, 4111-4122.
- Kelley, L.A., Mezulis, S., Yates, C.M., Wass, M.N., Sternberg, M.J., 2015. The Phyre2 web portal for protein modeling, prediction and analysis. *Nat. Protoc.* 10, 845-858.
- Kieser, T., Bibb, M.J., Buttner, M.J., Chater, K.F., Hopwood, D.A., 2000. *Practical Streptomyces Genetics*. Norwich, UK: The John Innes Foundation, Crowes.
- Khuri, S., Bakker, F.T., Dunwell, J.M., 2001. Phylogeny, function, and evolution of the cupins, a structurally conserved, functionally diverse superfamily of proteins. *Mol. Biol. Evol.* 18, 593-605.
- Kim, J.J., Miura, R., 2004. Acyl-CoA dehydrogenases and acyl-CoA oxidases. Structural basis for mechanistic similarities and differences. *Eur. J. Biochem.* 271, 483-493.
- Kuhstoss, S., Huber, M., Turner, J.R., Paschal, J.W., Rao, R.N., 1996. Production of a novel polyketide through the construction of a hybrid polyketide synthase. *Gene* 183 (1-2), 231-236.
- Langmead, B., Salzberg, S.L., 2012. Fast gapped-read alignment with Bowtie 2. *Nat. Methods* 9, 357-359.
- Lapik, Y.R., Kaufman, L.S., 2003. The Arabidopsis cupin domain protein AtPirin1 interacts with the G protein alpha-subunit GPA1 and regulates seed germination and early seedling development. *Plant Cell* 15, 1578-1590.

- Lauchnor, E.G., Radniecki, T.S., Semprini, L., 2011. Inhibition and gene expression of *Nitrosomonas europaea* biofilms exposed to phenol and toluene. *Biotechnol. Bioeng.* 108, 750-757.
- Lea, W., Abbas, A.S., Sprecher, H., Vockley, J., Schulz, H., 2000. Long-chain acyl-CoA dehydrogenase is a key enzyme in the mitochondrial L-oxidation of unsaturated fatty acids. *Biochim. Biophys. Acta* 1485, 121-128.
- Lee, H., Park, H., Ko, J., Seok, C., 2013. GalaxyGemini: a web server for protein homo-oligomer structure prediction based on similarity. *Bioinformatics* 29, 1078-1080.
- Le Maréchal, P., Decottignies, P., Marchand, C.H., Degrouard, J., Jaillard, D., Dulermo, T., Froissard, M., Smirnov, A., Chapuis, V., Virolle, M.J., 2013. Comparative proteomic analysis of *Streptomyces lividans* Wild-Type and *ppk* mutant strains reveals the importance of storage lipids for antibiotic biosynthesis. *Appl. Environ. Microbiol.* 79, 5907-5917.
- Li, H., Handsaker, B., Wysoker, A., Fennell, T., Ruan, J., Homer, N., Marth, G., Abecasis, G., Durbin, R.; 1000 Genome Project Data Processing Subgroup, 2009. The sequence alignment/map format and SAMtools. *Bioinformatics* 25, 2078–2079.
- Liu, F., Rehmani, I., Esaki, S., Fu, R., Chen, L., de Serrano, V., Liu, A., 2013. Pirin is an iron-dependent redox regulator of NF- κ B. *Proc. Natl. Acad. Sci. U.S.A.* 110, 9722–9727.
- Love, M.I., Huber, W., Anders, S., 2014. Moderated estimation of fold change and dispersion for RNA-seq data with DESeq2. *Genome Biol.* 15, 550.
- Lovell, S.C., Davis, I.W., Arendall, W.B., 3rd, de Bakker, P.I., Word, J.M., Prisant, M.G., Richardson, J.S., Richardson, D.C., 2003. Structure validation by Calpha geometry: phi, psi and Cbeta deviation. *Proteins* 50, 437-450.
- Marchler-Bauer, A., Derbyshire, M.K., Gonzales, N.R., Lu, S., Chitsaz, F., Geer, L.Y., Geer, R.C., He, J., Gwadz, M., Hurwitz, D.I., Lanczycki, C.J., Lu, F., Marchler, G.H., Song, J.S., Thanki, N., Wang, Z., Yamashita, R.A., Zhang, D., Zheng, C., Bryant, S.H., 2015. CDD: NCBI's conserved domain database. *Nucleic Acids Res.* 43, D222-D226.

- Mashiach, E., Schneidman-Duhovny, D., Andrusier, N., Nussinov, R., Wolfson, H.J., 2008. FireDock: a web server for fast interaction refinement in molecular docking. *Nucleic Acids Res.* 36, W229-W232.
- Millan-Oropeza, A., Henry, C., Blein-Nicolas, M., Aubert-Frambourg, A., Moussa, F., Bleton, J., Virolle, M.J., 2017a. Quantitative proteomics analysis confirmed oxidative metabolism predominates in *Streptomyces coelicolor* versus glycolytic metabolism in *Streptomyces lividans*. *J. Proteome Res.* 16, 2597-2613.
- Millan-Oropeza, A., Rebois, R., David, M., Moussa, F., Dazzi, A., Bleton, J., Virolle, M.J., Deniset-Besseau, A., 2017b. Attenuated Total Reflection Fourier Transform Infrared (ATR FT-IR) for rapid determination of microbial cell lipid content: correlation with Gas Chromatography-Mass Spectrometry (GC-MS). *Appl. Spectrosc.* 71, 2344-2352.
- Mills, J.E., Dean, P.M., 1996. Three-dimensional hydrogen-bond geometry and probability information from a crystal survey. *J. Comput. Aided Mol. Des.* 10, 607-622.
- Moreno, M., Silvestri, E., De Matteis, R., de Lange, P., Lombardi, A., Glinni, D., Senese, R., Cioffi, F., Salzano, A.M., Scaloni, A., Lanni, A., Goglia, F., 2011. 3,5-Diiodo-L-thyronine prevents high-fat-diet-induced insulin resistance in rat skeletal muscle through metabolic and structural adaptations. *FASEB J.* 25, 3312-3324.
- Murakami, Y., Mizuguchi, K., 2010. Applying the Naïve Bayes classifier with kernel density estimation to the prediction of protein-protein interaction sites. *Bioinformatics* 26, 1841-1848.
- Neubauer, S., Chu, D.B., Marx, H., Sauer, M., Hann, S., Koellensperger, G., 2015. LC-MS/MS-based analysis of coenzyme A and short-chain acyl-coenzyme A thioesters. *Anal. Bioanal. Chem.* 407, 6681-6688.
- Nueda, M.J., Tarazona, S., Conesa, A., 2014. Next maSigPro: updating maSigPro 37ioconductor package for RNA-seq time series. *Bioinformatics* 30, 2598-2602.

- Ochi, K., 1987. Metabolic initiation of differentiation and secondary metabolism by *Streptomyces griseus*: significance of the stringent response (ppGpp) and GTP content in relation to A factor. *J. Bacteriol.* 169, 3608–3616.
- Onaka, H., Taniguchi, S., Ikeda, H., Igarashi, Y., Furumai, T., 2003. pTOYAMAcos, pTYM18, and pTYM19, actinomycete-*Escherichia coli* integrating vectors for heterologous gene expression. *J. Antibiot. (Tokyo)* 56, 950–956.
- Orzaez, D., de Jong, A.J., Woltering, E.J., 2001. A tomato homologue of the human protein PIRIN is induced during programmed cell death. *Plant Mol. Biol.* 46, 459–468.
- Palazzotto, E., Gallo, G., Renzone, G., Giardina, A., Sutura, A., Silva, J., Vocat, C., Botta, L., Scaloni, A., Puglia, A.M., 2016. TrpM, a small protein modulating tryptophan biosynthesis and morpho-physiological differentiation in *Streptomyces coelicolor* A3(2). *PLoS One* 11, e0163422.
- Pang, H., Bartlam, M., Zeng, Q., Miyatake, H., Hisano, T., Miki, K., Wong, L.L., Gao, G.F., Rao, Z., 2004. Crystal structure of human Pirin: an iron binding nuclear protein and transcription cofactor. *J. Biol. Chem.* 279, 1491-1498.
- Pettersen, E.F., Goddard, T.D., Huang, C.C., Couch, G.S., Greenblatt, D.M., Meng, E.C., Ferrin, T.E., 2004. UCSF Chimera--a visualization system for exploratory research and analysis. *J. Comput. Chem.* 25, 1605-1612.
- Pinatel, E., Peano, C., 2018. RNA sequencing and analysis in microorganisms for metabolic network reconstruction. *Methods Mol. Biol.* 1716, 239-265.
- Puglia, A.M., Vohradsky, J., Thompson, C.J., 1995. Developmental control of the heat-shock stress regulon in *Streptomyces coelicolor*. *Mol. Microbiol.* 17, 737-746.
- Quinlan, A.R., Hall, I.M., 2010. BEDTools: a flexible suite of utilities for comparing genomic features. *Bioinformatics* 26, 841-842.
- Sambrook, J., Russell, D.W., 2001. *Molecular Cloning. A Laboratory Manual*. Cold Spring Harbor Laboratory Press, Cold Spring Harbor, New York.

- Schauner, C., Dary, A., Lebrihi, A., Leblond, P., Decaris, B., Germain, P., 1999. Modulation of lipid metabolism and spiramycin biosynthesis in *Streptomyces ambofaciens* unstable mutants. *Appl. Environ. Microbiol.* 65, 2730-2737.
- Schujman, G.E., de Mendoza, D., 2008. Regulation of type II fatty acid synthase in Gram-positive bacteria. *Curr. Opin. Microbiol.* 11 (2), 148-152.
- Scippa, G.S., Rocco, M., Iallicco, M., Trupiano, D., Viscosi, V., Di Michele, M., Arena, S., Chiatante, D., Scaloni A., 2010. The proteome of lentil (*Lens culinaris* Medik.) seeds: discriminating between landraces. *Electrophoresis* 31, 497-506.
- Seifert, E.L., Estey, C., Xuan, J.Y., Harper, M.E., 2010. Electron transport chain-dependent and -independent mechanisms of mitochondrial H₂O₂ emission during long-chain fatty acid oxidation. *J. Biol. Chem.* 285, 5748-5758.
- Smith, M.C.M., Brown, W.R.A., McEwan, A.R., Rowley, P.A., 2010. Site-specific recombination by Φ C31 integrase and other serine recombinases. *Biochem. Soc Trans.* 38, 388–394.
- Soo, P.C., Horng, Y.T., Lai, M.J., Wei, J.R., Hsieh, S.C., Chang, Y.L., Tsai, Y.H., Lai, H.C., 2007. Pirin regulates pyruvate catabolism by interacting with the pyruvate dehydrogenase E1 subunit and modulating pyruvate dehydrogenase activity. *J. Bacteriol.* 189, 109-118.
- Tani, A., Ishige, T., Sakai, Y., Kato, N., 2002. Two acyl-CoA dehydrogenases of *Acinetobacter* sp. Strain M-1 that uses very long-chain n-alkanes. *J. Biosci. Bioeng.* 94, 326-329.
- Thibessard, A., Haas, D., Gerbaud, C., Aigle, B., Lautru, S., Pernodet, J.L., Leblond, P., 2015. Complete genome sequence of *Streptomyces ambofaciens* ATCC 23877, the spiramycin producer. *J. Biotechnol.* 214, 117-118.
- Tovchigrechko, A., Vakser, I.A., 2006. GRAMM-X public web server for protein–protein docking. *Nucleic Acids Res.* 34, W310-W314.
- Wass, M.N., Kelley, L.A., Sternberg, M.J., 2010. 3DLigandSite: predicting ligand-binding sites using similar structures. *Nucleic Acids Res.* 38, W469-W473.

- Wei, Z.H., Bai, L., Deng, Z., Zhong J.J., 2011. Enhanced production of validamycin A by H₂O₂-induced reactive oxygen species in fermentation of *Streptomyces hygroscopicus* 5008. *Bioresour. Technol.* 102, 1783-1787.
- Wendler, W.M., Kremmer, E., Forster, R., Winnacker, E.L., 1997. Identification of pirin, a novel highly conserved nuclear protein. *J. Biol. Chem.* 272, 8482–8489.
- Yang, J., Yan, R., Roy, A., Xu, D., Poisson, J., Zhang, Y. 2015. The I-TASSER Suite: Protein structure and function prediction. *Nat. Methods* 12, 7-8.
- Zhang, H., Boghigian, B.A., Pfeifer, B.A., 2010. Investigating the role of native propionyl-CoA and methylmalonyl-CoA metabolism on heterologous polyketide production in *Escherichia coli*. *Biotechnol. Bioeng.* 105, 567-573.

Figure legends

Fig. 1. Colony phenotype and grey pigmentation of surface mycelium of *S. ambofaciens* wild type, *pirA::pTYM-18* and complemented *pirA::pTYM-pirA* strains. (A) Top panels show the strains streaked on SM-II agar and incubated for 168 h. Middle panels illustrate details of colonies from enlargements of the corresponding top panels. In the bottom panels, the strains were streaked to confluence on SM-II agar, and incubated for 168 h. Then reflectance spectra were determined (B). Data represent means \pm standard deviations from three independent experiments.

Fig. 2. Growth curves, spiramycin production and total lipid content. *S. ambofaciens* wild type, *pirA::pTYM-18* and *pirA::pTYM-pirA* strains were cultivated in YS broth at different time points. Then biomass (A), spiramycin production (C), and total lipid content estimated as CO/amide I ratio by ATR-FTIR spectroscopy (E) were determined. Biomass (B) and spiramycin production (D) from bacteria cultivated in SFM broth.

Fig. 3. Analysis of intracellular short-chain acyl-CoA pools. *S. ambofaciens* wild type, *pirA::pTYM-18* and *pirA::pTYM-pirA* were cultivated in YS broth and the intracellular pool of acetyl-CoA, acetoacetyl-CoA, malonyl-CoA, methylmalonyl-CoA, propionyl-CoA, butyryl-CoA, crotonyl-CoA and ethylmalonyl-CoA was determined at different time points by reverse-phase HPLC-ESI-MS/MS.

Fig. 4. Transcription modulation of genes involved in central (and energy) and lipid metabolism. Genes up-regulated (red) or down-regulated (green) in *pirA::pTYM-18* as compared to wild type strain are shown as inferred from maSigPro analysis of RNA-Seq data. Short-chain acyl-CoA pools that were assayed are boxed in boldface; blue upward arrows indicate enhanced abundance in the *pirA* mutant compared to the wild type strain; blue downward arrows indicate reduced abundance in the *pirA* mutant compared to the wild type strain; blue horizontal arrows indicate temporal shift in

abundance in the *pirA* mutant compared to the wild type strain; blue sign = indicate no change between *pirA* mutant and wild type strain.

Fig. 5. Survival of *S. ambifaciens* wild type and *pirA*::pTYM-18 strains after exposure to H₂O₂. *S. ambifaciens* cultures were treated with H₂O₂ at different concentration for 1 h at 30 °C, before cells were harvested by centrifugation and plated on YS agar for the count. Data represent means ± standard deviations from three independent experiments.

Fig. 6. *In silico* interaction between PirA and vLCAD AcdB. (A) 3D models of proteins from deduced amino acid sequences of PirA (RS18305) (left) and AcdB (RS18295) (right) were generated by I-Tasser Suite. AcdB homo-dimerization (right) was predicted and modeled by Gemini-GalaxyWEB. (B) Secondary structure analysis of AcdB was carried out by using I-Tasser for helix and strand prediction. Tmpred was used for prediction of transmembrane regions and orientation. DLP-SVM was used as a domain linker predictor. ConSurf server was used for estimation and visualization of evolutionary conservation of amino acids. Gramm-X was used to obtain contact residues of AcdB in complex with PirA. PSiver was used to predict the binding interface and to filtrate residues previously individuated by Gramm-X. (C) Interaction between AcdB and acyl-CoA substrates was analyzed by SwissDock. (D) 3D models showing contact residues between PirA and AcdB. PirA regions contacting AcdB are depicted in yellow (left). AcdB regions contacting PirA are indicated in red, binding residues for substrate and cofactor are indicated in cyan, and contact residues between monomer A and B of AcdB are indicated in fuchsia (right). (E) 3D model of PirA-Ac dB complex was obtained by Chimera. The image shows contact regions between PirA and Ac dB monomer (red), Ac dB regions involved in FAD and acyl-CoA binding (cyan), and Ac dB homo-dimerization residues (fuchsia). The metal-binding domain of PirA is near to Ac dB active site.

Fig. 7. *In vitro* interaction between PirA and vLCAD AcdB, and corresponding AcdB enzymatic activity. (A) *In vitro* interaction between AcdB and PirA. Physical interaction between tagged AcdB (AcdB-V5/His6) and PirA (PirA-V5) was assayed by co-elution experiments using affinity chromatography as detailed in the experimental section. Crude extract lysates from *E. coli* BL21(DE3) transformed with either pET-AcdB-V5/His6 (lane 1) or pET-PirA-V5 (lane 2) were used. V5-tagged proteins were detected by Western blotting using antibody against V5 epitope. In lane 3, the two extracts were mixed and challenged by affinity chromatography to detect AcdB-V5/His6:PirA-V5 complex formation. In lanes 4 and 5, extracts from *E. coli* BL21(DE3) transformed with either pET-AcdB-V5/His6 or pET-PirA-V5 were challenged with a control extract from *E. coli* BL21(DE3) transformed with pET-21b vector. (B) Palmitoyl-CoA activity of recombinant AcdB was determined either in absence or in the presence of a 5-fold molar excess of Fe(II)- or Fe(III)-PirA. Data represent means \pm standard deviations from three independent experiments.

Supplementary material

Supplementary Fig. 1. Microbiological assays of antibiotic production. *S. ambofaciens* wild type, *pirA::pTYM-18* and *pirA::pTYM-pirA* strains were cultivated on R2 agar and antibiotic production was analyzed at indicated time points using *Bacillus subtilis* as a tester microorganism. To better appreciate the growth inhibition halos around the agar disks with *S. ambofaciens* mycelium, photos were taken on both sides of the agar plates (top and bottom).

Supplementary Fig. 2. Antimycin production in SFM broth. *S. ambofaciens* wild type, *pirA::pTYM-18* and *pirA::pTYM-pirA* strains were cultivated in SFM broth and antimycin production was determined by HPLC at different time points (72, 120 and 168 h). The figure illustrates the chromatograms from the different samples, and the antimycin standard (on top). The latter is a mixture of components A₁, A₂, A₃ and A₄ (left), whose structure is also shown (right). Chromatogram peaks that refer to antimycin components are circled in red.

Supplementary Fig. 3. maSigPro analysis of RNA-Seq time series dataset. *S. ambofaciens* wild type and *pirA::pTYM-18* strains were cultivated in YS broth for 48, 72, 96 or 120 h (T1, T2, T3 and T4, respectively) for RNA-Seq analysis. Results from duplicated samples (a and b) were clustered by maSigPro. The expression pattern of 1600 variable genes during the time course subdivided into 9 clusters is shown (A). The median profile of each cluster was inferred from the expression patterns (B).

Supplementary Fig. 4. 2D-DIGE maps of the whole protein extracts. Representative 2D-DIGE proteomic maps of *S. ambofaciens pirA::pTYM-18* (A) and wild type (B) strains after 120 h of growth. In A, labels refer to differentially represented protein species. In particular, 2D-DIGE analysis revealed 26 differentially represented protein spots, with 19 and 7 ones down- and over-represented in *pirA*-defective with respect to wild type strain, respectively. A combination of

nanoLC-ESI-LIT-MS/MS experiments was carried out to obtain protein identification (see Supplementary Tables 2 and 3 for details). When subjected to MS analysis, 23 spots were univocally associated with a single migrating component; thus, they corresponded to the product of 22 genes, with only *lpd* product identified in two spots (Supplementary Table 2). Remaining 3 protein spots were associated with multiple protein identifications (Supplementary Table 3).

Supplementary Fig. 5. ATR-FTIR spectra of *S. ambofaciens* wild type (A) *pirA*::pTYM-18 (B) and *pirA*::pTYM-*pirA* (C) strains cultivated in YS broth and harvested at indicated time points.

Supplementary Fig. 6. Cluster analysis of the *S. ambofaciens* ACADs and structural features of AcdB-3855. (A) Cluster analysis of deduced amino acid sequences of *S. ambofaciens* ACADs was carried out by ClusterW. Numbers refer to RefSeq (RS) number in the annotated genome sequence of *S. ambofaciens* ATCC 23877. ACAD-encoding genes that were up-regulated (red) or down-regulated (green) in *pirA*::pTYM-18 as compared to wild type strain are shown. Cluster analysis was refined by Conserved Domain database to deduce putative ACAD functions. SCAD, short-chain acyl-CoA dehydrogenase; LCAD, long-chain acyl-CoA dehydrogenase; vLCAD, very long-chain acyl-CoA dehydrogenase; GCAD, glutaryl-CoA dehydrogenase; PCAD, pimeloyl-CoA dehydrogenase; iVCAD, isovaleryl-CoA dehydrogenase; AlpO, alpomyacin cluster-associated gene; Srm35, spiramycin cluster-associated gene; SfnB, ACAD with sulfate starvation induced SfnB domain. (B) Structural homologies between AcdB (RS18295) from *S. ambofaciens* ATCC 23877 and AcdB from *Acinetobacter* sp. strain M-1 as inferred from BLASTP-Conserved Domain (top) and TMMOD (bottom) analyses.

Supplementary Fig. 7. Genetic map of the four *pirA*-containing loci of *S. ambofaciens*, and expression of *pirA* paralogs. (A) Genetic map of the four *pirA*-containing loci of *S. ambofaciens* ATCC 23877. Numbers refer to RefSeq (RS) number in the annotated genome sequence of *S.*

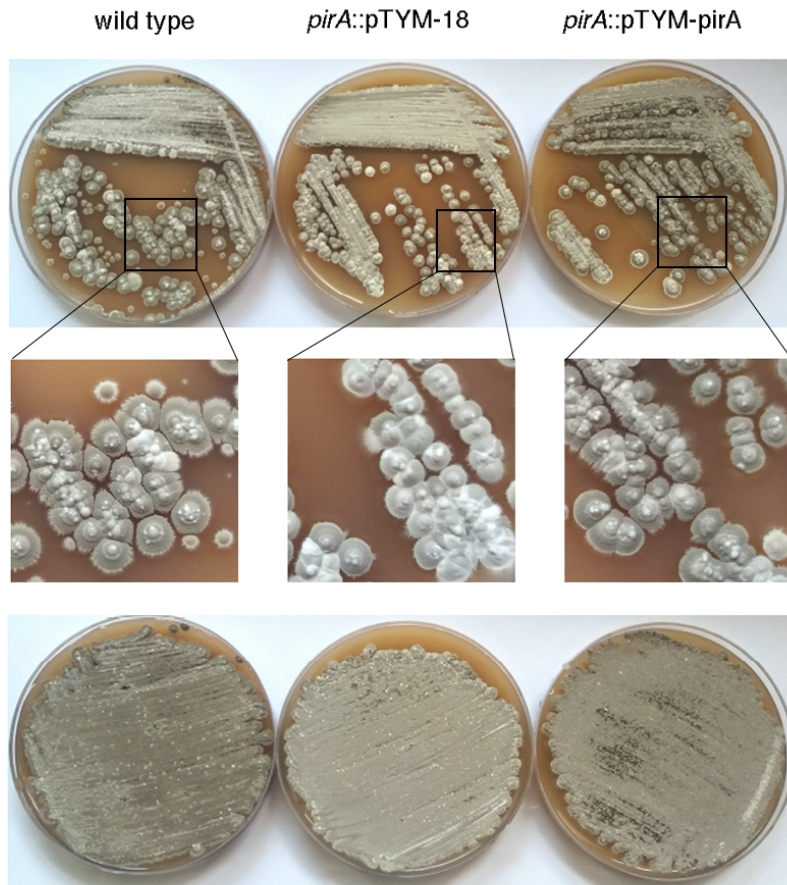
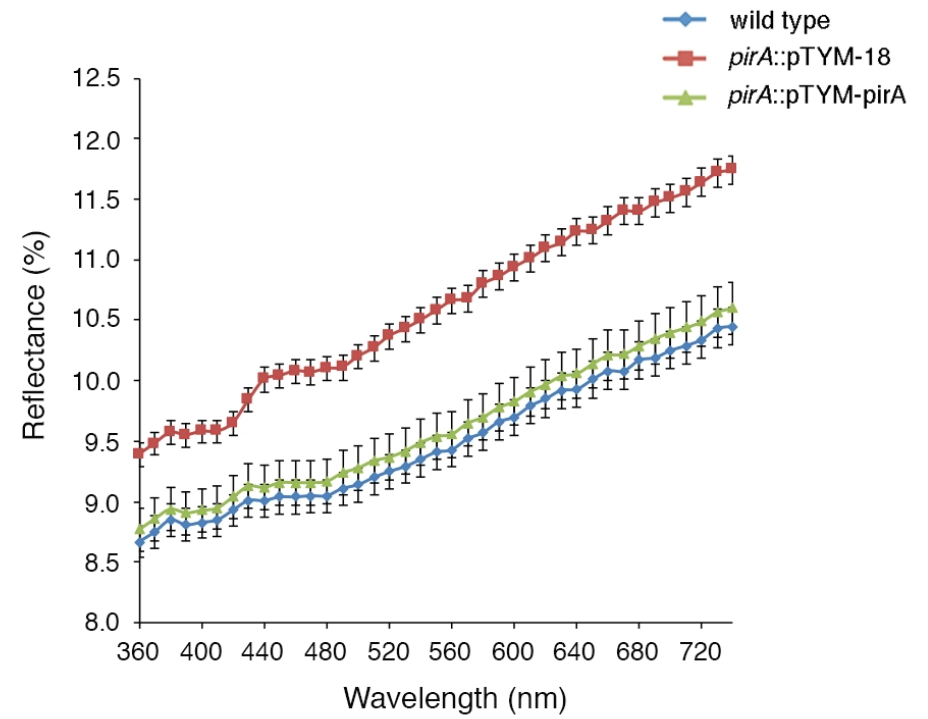
ambofaciens ATCC 23877. (B) Expression of *pirA* paralogs (*pirA*, *pirA2*, *pirA3* and *pirA4*) in *S. ambofaciens* ATCC 23877 grown in YS broth at different time points, as inferred by RNAseq data.

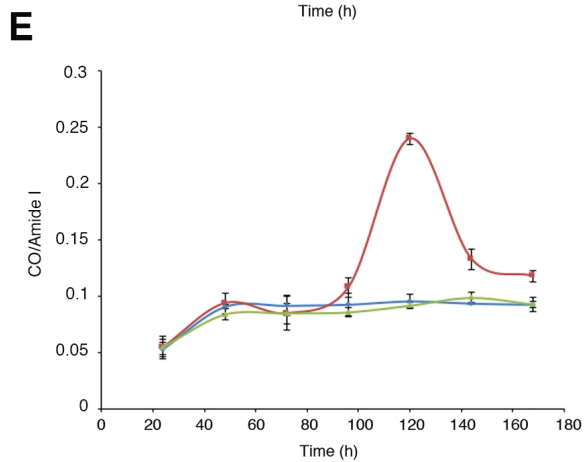
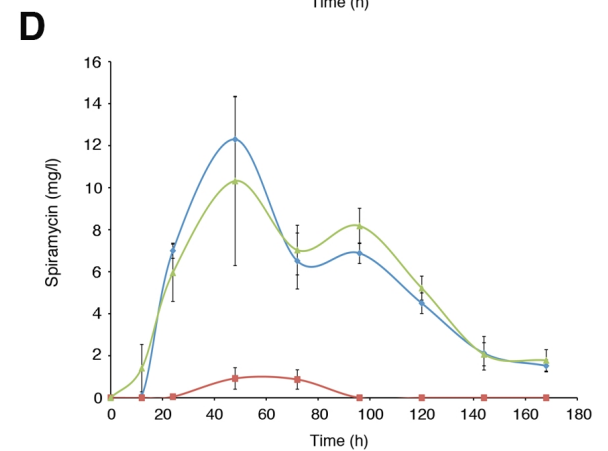
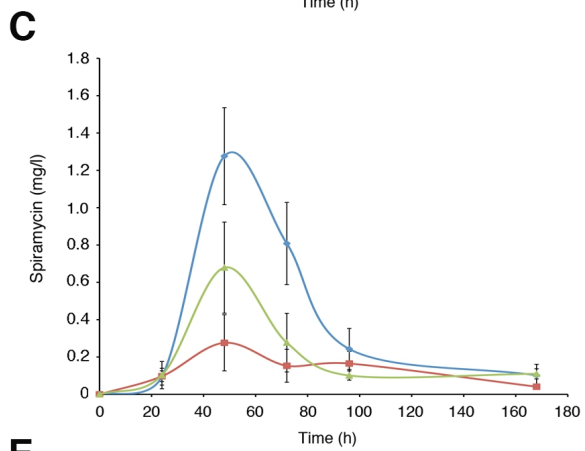
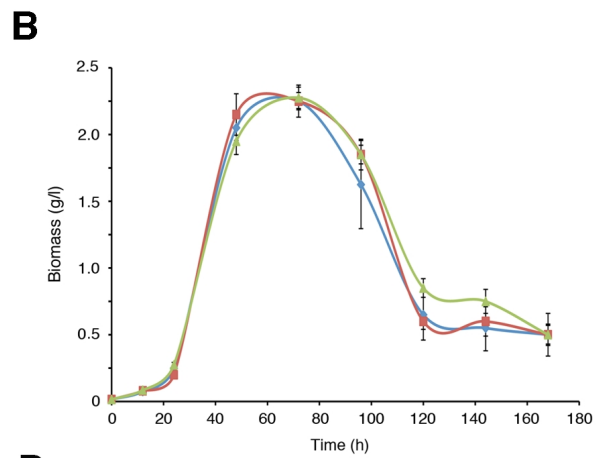
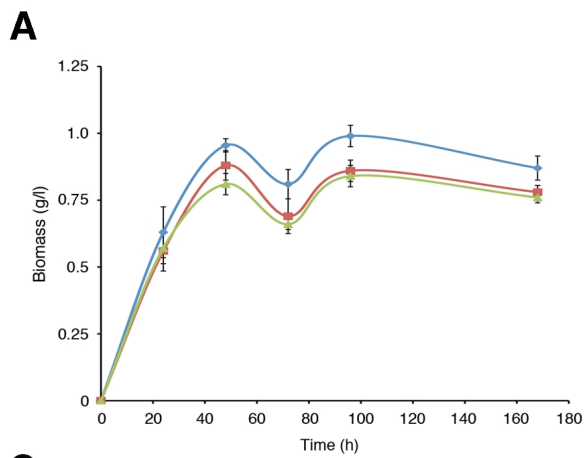
Supplementary Fig. 8. Purification of recombinant AcdB-V5/His6 and pET-PirA-V5 proteins. SDS-PAGE analyses of crude extracts lysates (L) from *E. coli* BL21(DE3) competent cells transformed with either pET-AcdB-V5/His6 (lane 2, left) or pET-PirA-V5 (lane 2, right), respective pass-through fractions (PT) (lane 3, left and right), resin washing (W) (lane 4, left and right), and eluted (E) proteins (lane 5, left and right) are shown. Molecular mass ladders were run in parallel (lane 1, left and right). Molecular mass values of eluted proteins are reported on the right of each panel.

Supplementary Table 1. maSigPro analysis of RNA-Seq time series dataset.

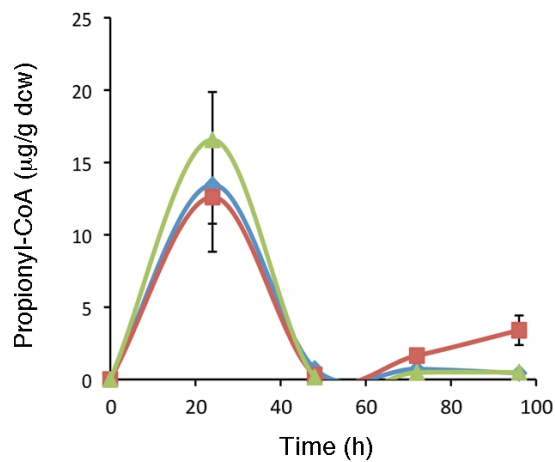
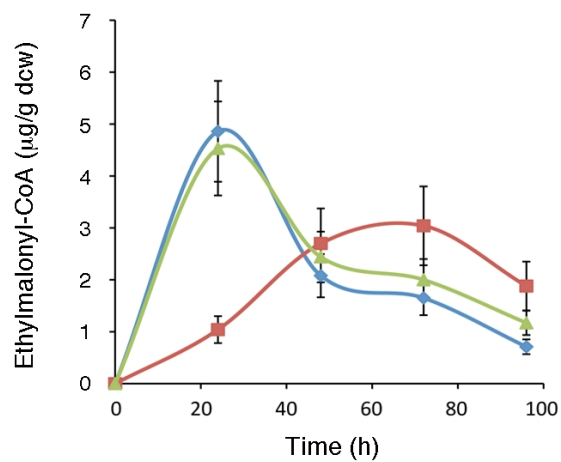
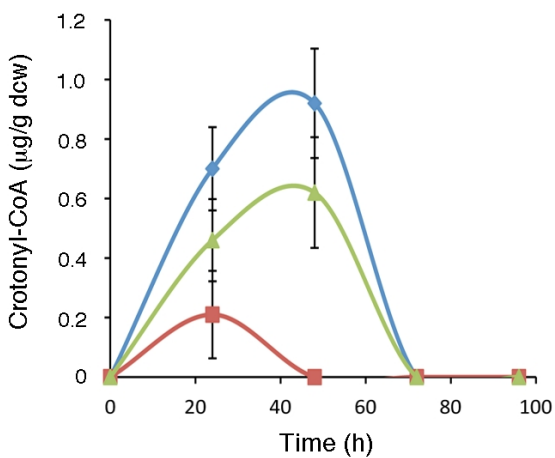
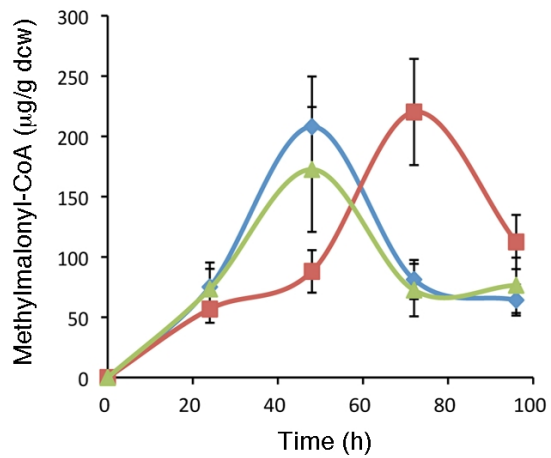
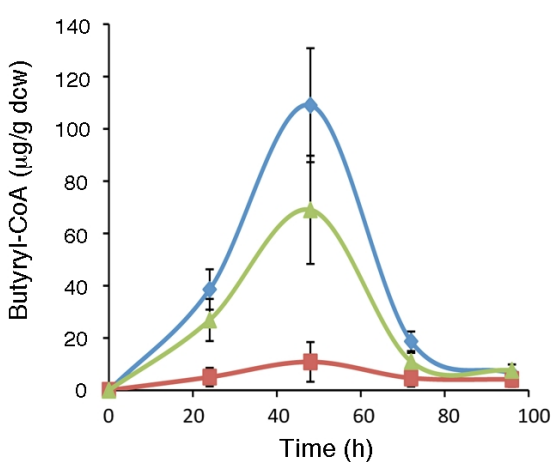
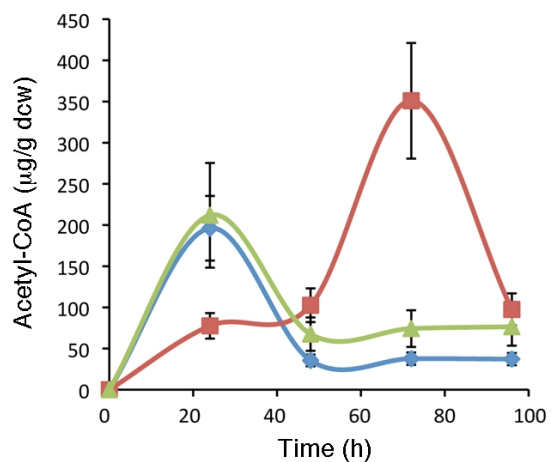
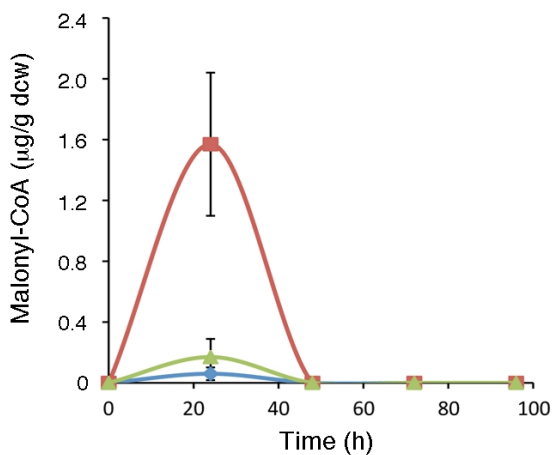
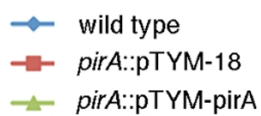
Supplementary Table 2. Differentially abundant protein species revealed by proteomic comparison between *S. ambofaciens* wild type and *pirA*::pTYM-18 strains.

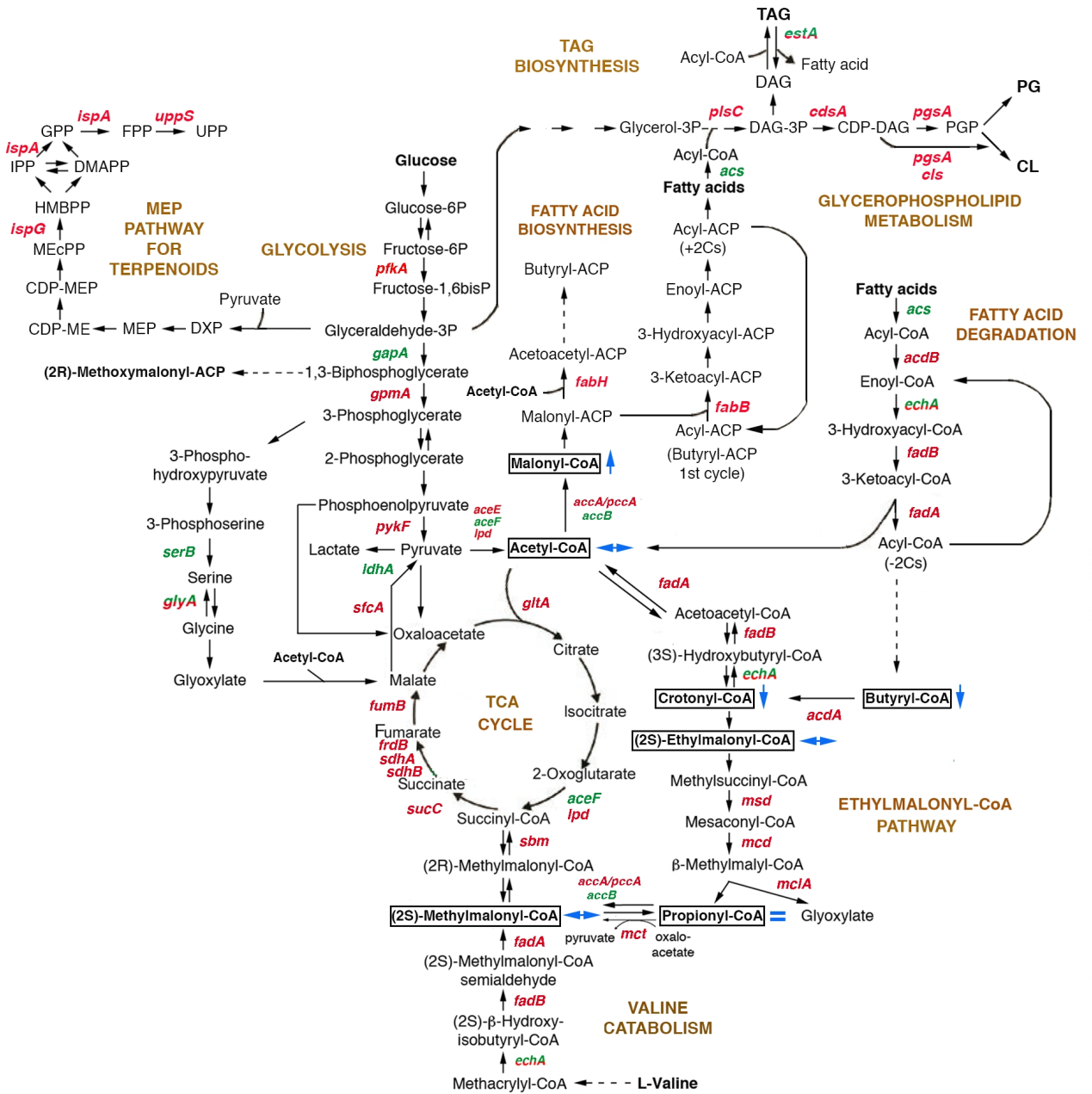
Supplementary Table 3. Gel spots having a differential representation during proteomic comparison between *S. ambofaciens* wild type and *pirA*::pTYM-18 strains but containing multiple comigrating protein species.

A**B**

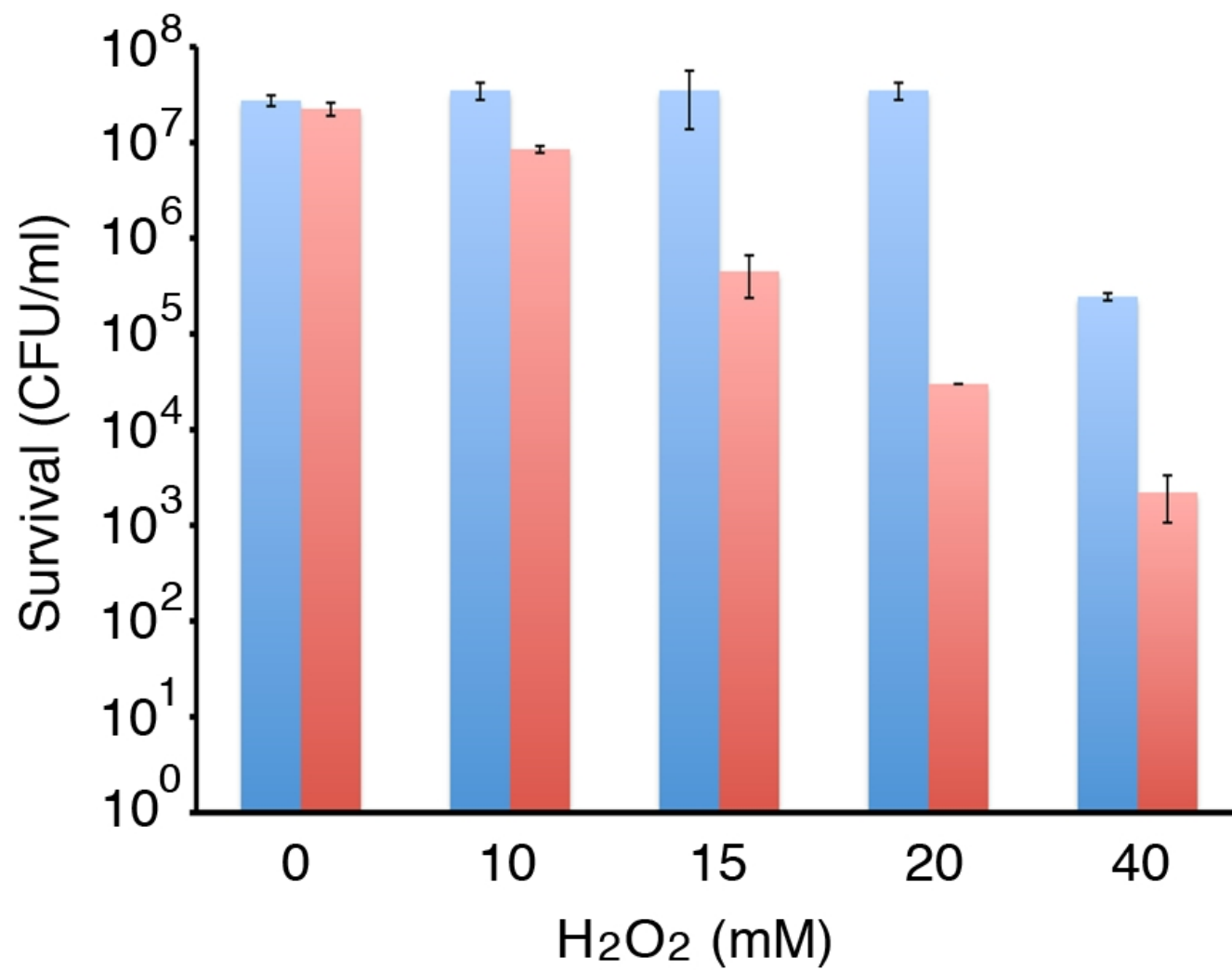


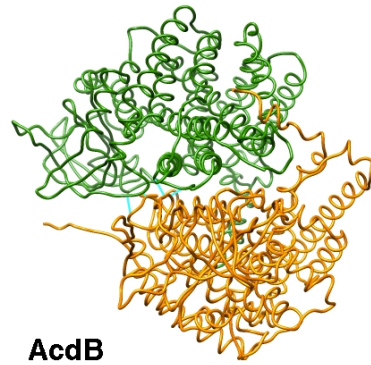
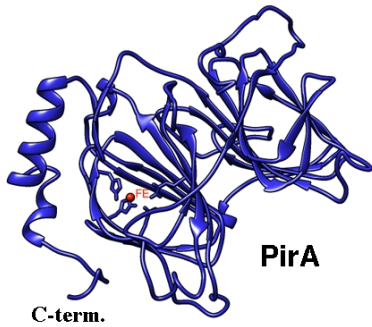
◆ wild type
■ *pirA::pTYM-18*
▲ *pirA::pTYM-pirA*





- wild type
- *pirA*::pTYM-18



A**B**

CCCCCCCCCCCCCCCCHHHHHHHHHHHCCHHHHHCCCCCCCCCHHHHHHHHHHHHHHHHHHHHHHHCCCCCHHHCC
 MPRRSLNGAVAMGHYKPNLRDIEFNLFVFLGRDKVYGTGPPFAEMDTDATAKSVLEELTRLSENELAESFADADR
 DADR
 DADR

CCCCCCCCSSSSCCHHHHHHHHHHHCCCCCCCCCHCCCCCHHHHHHHHHHHHHHHHHHHHHHHHHHHHHHHHHHH
 NPPVFDPETNTAPVPASFKKSYQAFMDSEYWRGLPEIIGTTSPRSLIWAYAELILGANPAVVMYSSGPAFA
 NPPVFDPETNTAPVPASFKK LIWAYAELILGANPAVVMY
 NPPVFDPETNTAPVPASFKK LIWAYAELILGANPAVVMY

HHHHHHCHHHHHHHHHHHCCCCSSSSSSCCCCCCCCCHHHCCCCSSSSSSCCCCSSSSSSSSSSSSCCCCCCCCCS
 GILFEEGNEVQKHIAIASEVKEQWGSTMLVTEPDAGSDVAGRTKAVQQEDGSGWHIEGVKRFITSGEHDMSENI

SSSSSSCCCCCCCCSSSSSSSSCCCCCCCCCCCCCCCCSSSSCCCCCCCCCCCCSSSSSSCCCCCHHHCC
 LHVYLARPEGAGPCTKGLSLFLVPKYEFDFETGELGERNGVYATNVEHKMGLKASNTCEMTFGDRHPAKGWLI
 RPEGAGPCTKGL
 RPEGAGPCTKGL

CCCCHH
 GDKHDGIRQMFRIIEFARMVGTKAISTLSTGYLNALEYAKERVQGPDLANFMDKTA PKVTITHPDVRRLM

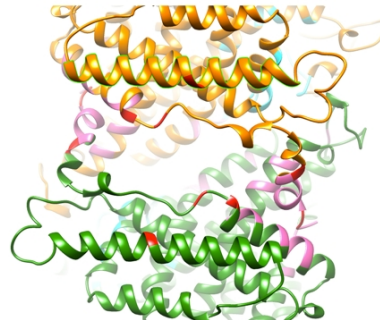
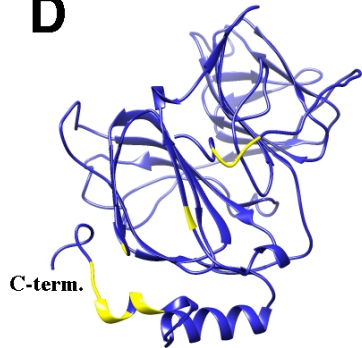
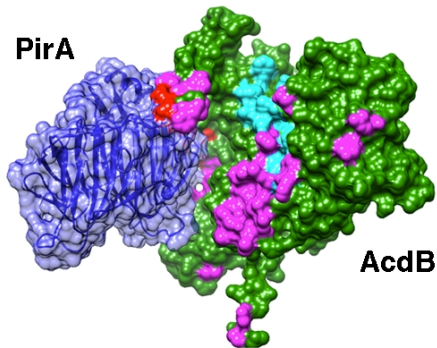
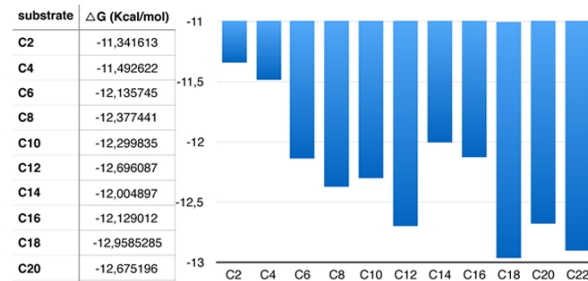
L D
 L D
 L D

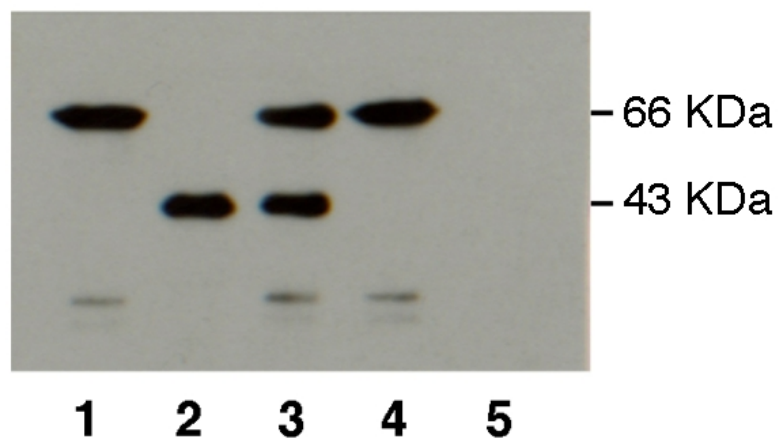
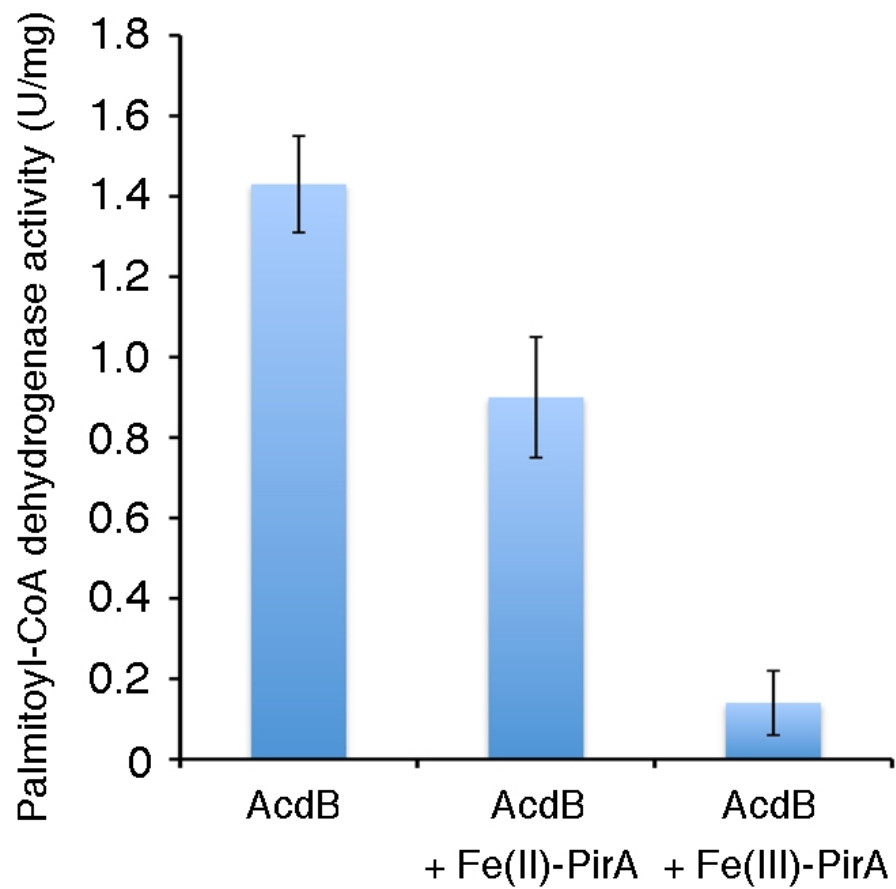
HH
 TQKAYAEGRALVMTASVQDEIQVKEANGEDAAATEHALNDLLPIVKGYGSEKAYEQLAQSQTFFGSGFLQ

CCHH
 EYPTEQYIRDAKIDTLYEGTFTAIQGDYFFRKIVRNQGAALNSLAEDIKKFLALATGGEELAGAREHLAKAAV
 ▲ A
 A
 A

HH
 ELEAIVGVMLTDLAATEQDVKNIIYKVLNTRLLLASGDVIVGYLLKGAAIAAEKLPATASAKDKAFYTGKIA
 E LLLASGDVIVGYLLKGAAIAA IA
 E LLLASGDVIVGYLLKGAAIAA IA

HH
 AAKFFAANVLPGLTLARKVAQGVLDLMELDEAAF E EA I-Tasser: Helix, Strand
 AAKFFAANVLPGLTLA E EA TMPRED: Transmembrane DLP-SVM: Linker
 A V P L T E EA PSIVER
 AAKFFAANVLPGLTLA E EA GRAMMX
 ConSurf: Conserved aa, scale: 1 2 3 4 5 6 7 8 9

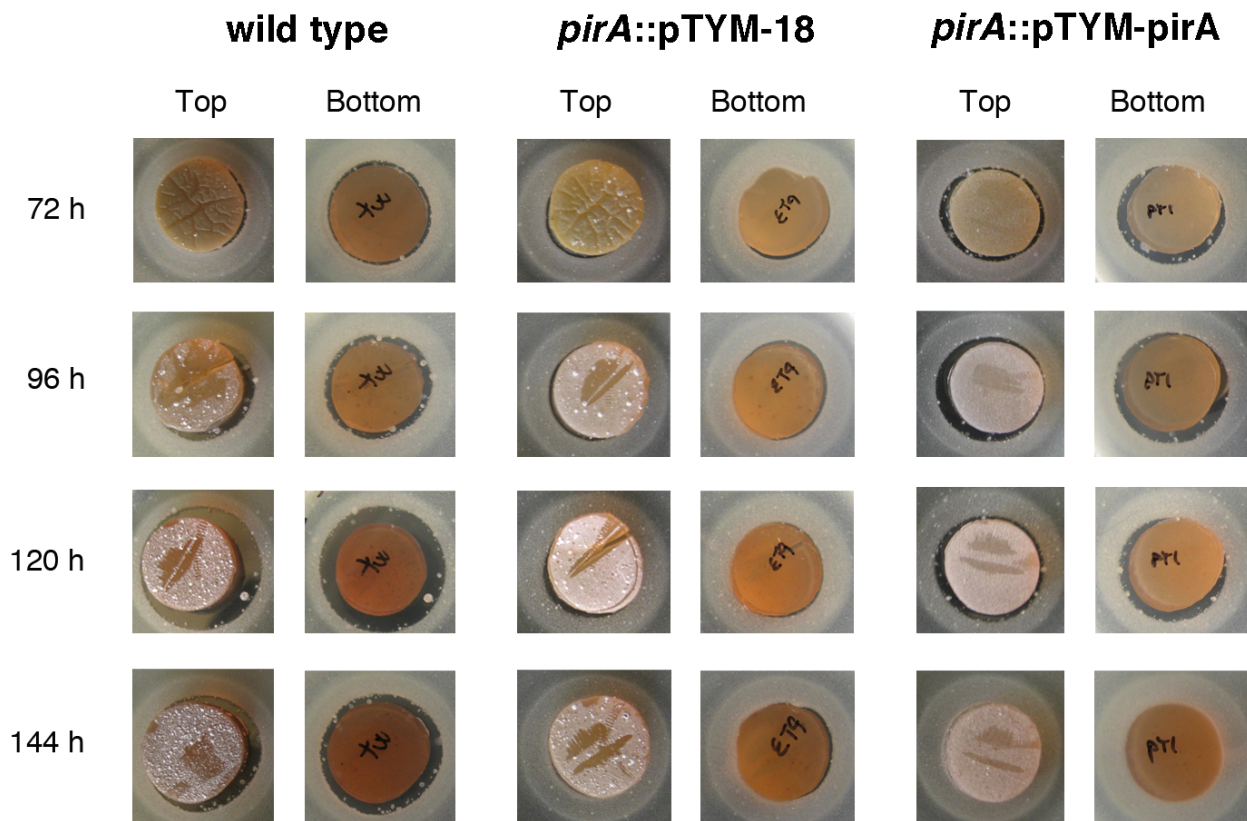
D**E****C**

A**B**

Pirin: a novel redox-sensitive modulator of primary and secondary metabolism in
Streptomyces

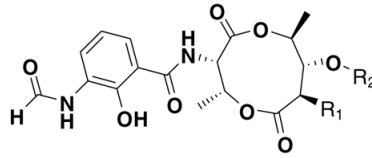
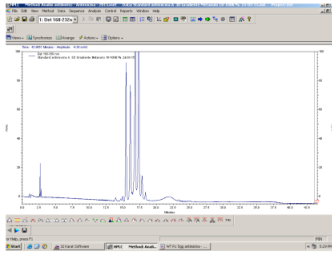
Adelfia Talà, Fabrizio Damiano, Giuseppe Gallo, Eva Pinatel, Matteo Calcagnile, Mariangela Testini, Daniela Fico, Daniela Rizzo, Alberto Sutura, Giovanni Renzone, Andrea Scaloni, Gianluca De Bellis, Luisa Siculella, Giuseppe Egidio De Benedetto, Anna Maria Puglia, Clelia Peano and Pietro Alifano

SUPPLEMENTARY FIGURES



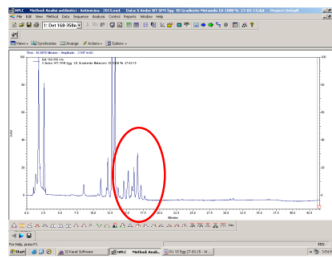
Supplementary Fig. 1. Microbiological assays of antibiotic production. *S. ambofaciens* wild type, *pirA*::pTYM-18 and *pirA*::pTYM-*pirA* strains were cultivated on R2 agar and antibiotic production was analyzed at indicated time points using *Bacillus subtilis* as a tester microorganism. To better appreciate the growth inhibition halos around the agar disks with *S. ambofaciens* mycelium, photos were taken on both sides of the agar plates (top and bottom).

Antimycin standard

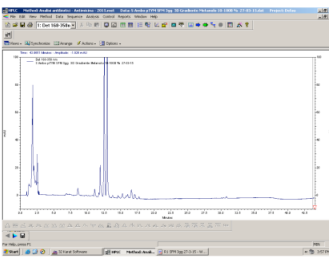


Antimycin A₁: R₁ -C₆H₁₃; R₂ -CO-C₄H₉
Antimycin A₂: R₁ -C₆H₁₃; R₂ -CO-C₃H₇
Antimycin A₃: R₁ -C₄H₉; R₂ -CO-C₄H₉
Antimycin A₄: R₁ -C₄H₉; R₂ -CO-C₃H₇

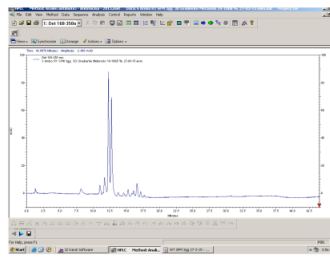
wild type (72 h)



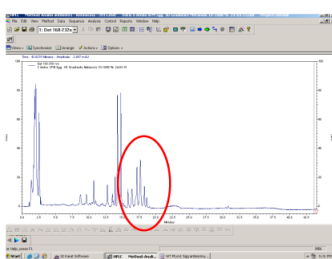
pirA::pTYM-18 (72 h)



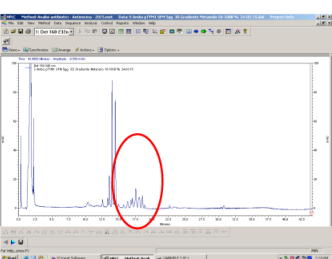
pirA::pTYM-pirA (72 h)



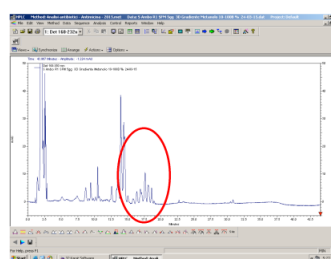
wild type (120 h)



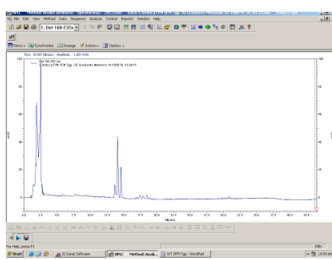
pirA::pTYM-18 (120 h)



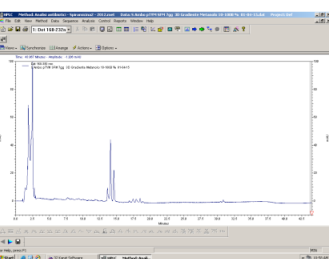
pirA::pTYM-pirA (120 h)



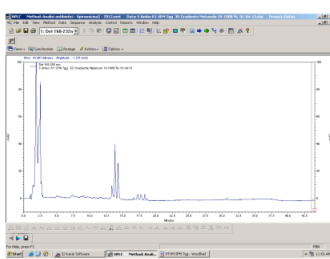
wild type (168 h)



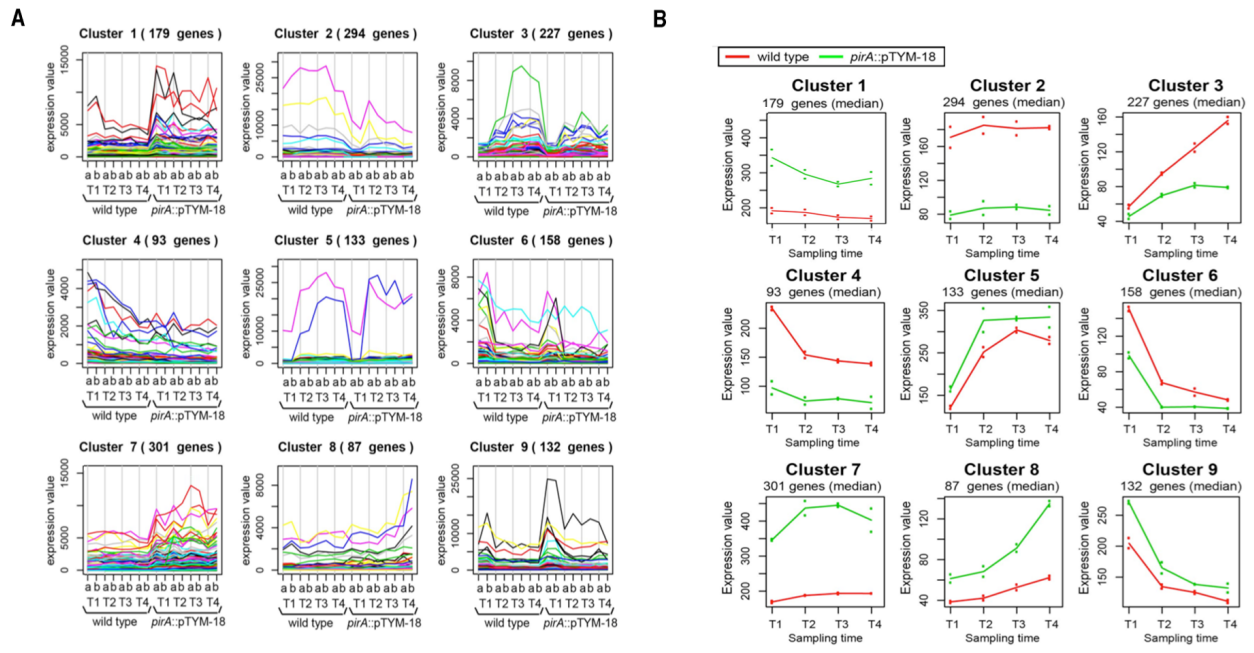
pirA::pTYM-18 (168 h)



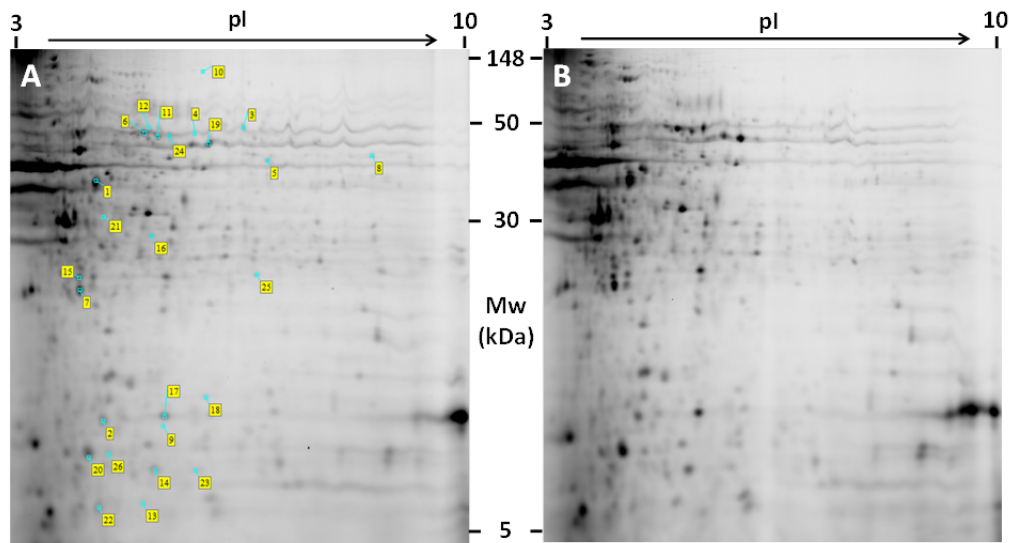
pirA::pTYM-pirA (168 h)



Supplementary Fig. 2. Antimycin production in SFM broth. *S. ambifaciens* wild type, *pirA::pTYM-18* and *pirA::pTYM-pirA* strains were cultivated in SFM broth and antimycin production was determined by HPLC at different time points (72, 120 and 168 h). The figure illustrates the chromatograms from the different samples, and (on top) the antimycin standard. The latter is a mixture of components A₁, A₂, A₃ and A₄ (left), whose structure is also shown (right). Chromatogram peaks that refer to antimycin components are circled in red.

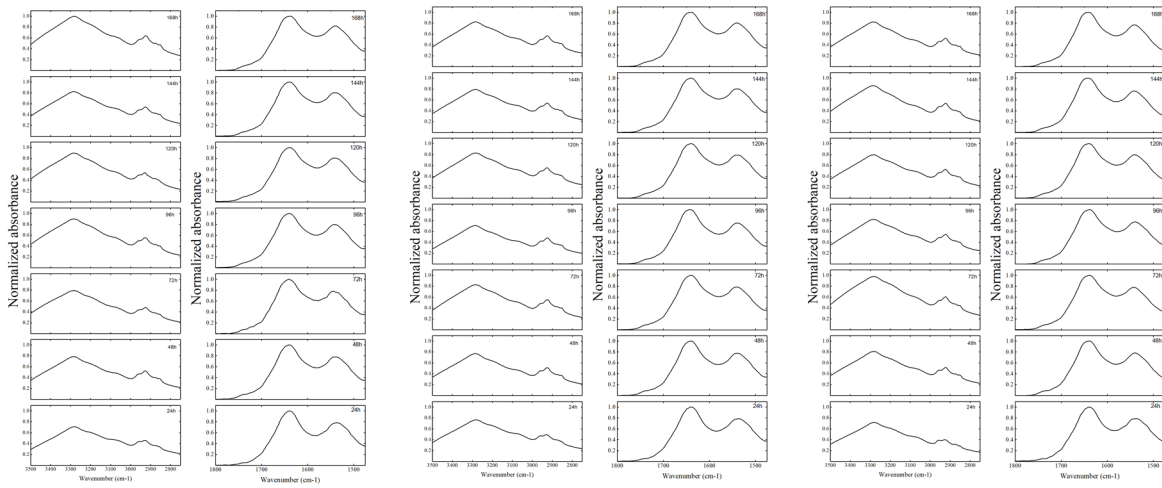


Supplementary Fig. 3. maSigPro analysis of RNA-Seq time series dataset. *S. ambifaciens* wild type and *pirA::pTYM-18* strains were cultivated in YS broth for 48, 72, 96 or 120 h (T1, T2, T3 and T4, respectively) for RNA-Seq analysis. Results from duplicated samples (a and b) were clustered by maSigPro. The expression pattern of 1604 variable genes during the time course subdivided into 9 clusters is shown (A). The median profile of each cluster was inferred from the expression patterns (B)

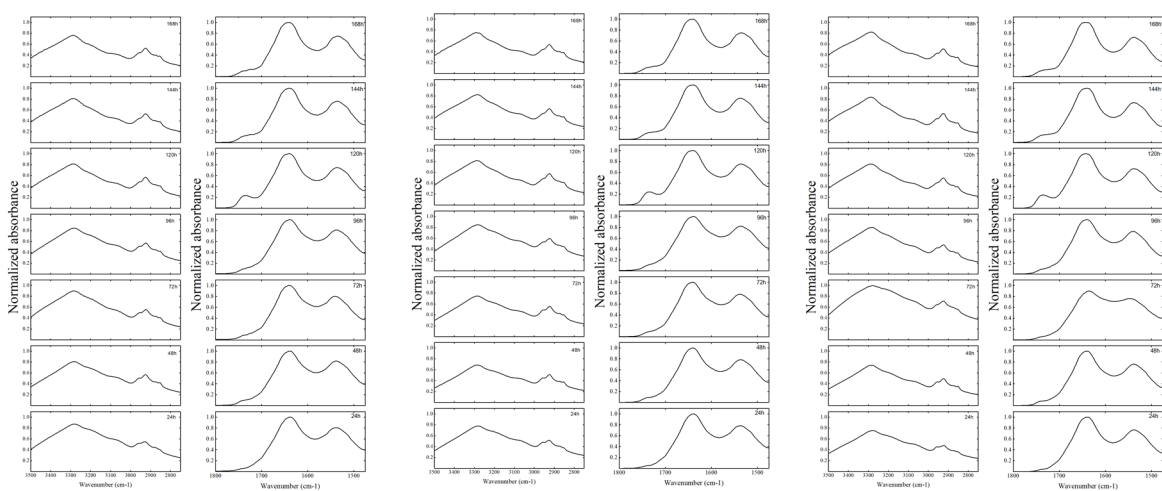


Supplementary Fig. 4. 2D-DIGE maps of the whole protein extracts. Representative 2D-DIGE proteomic maps of *S. ambofaciens* *pirA*::pTYM-18 (A) and wild type (B) strains after 120 h of growth. In A, labels refer to differentially represented protein species. In particular, 2D-DIGE analysis revealed 26 differentially represented protein spots, with 19 and 7 ones down- and over-represented in *pirA*-defective with respect to wild type strain, respectively. A combination of nanoLC-ESI-LIT-MS/MS experiments was carried out to obtain protein identification (see Supplementary Tables 2 and 3 for details). When subjected to MS analysis, 23 spots were univocally associated with a single migrating component; thus, they corresponded to the product of 22 genes, with only *lpd* product identified in two spots (Supplementary Table 2). Remaining 3 protein spots were associated with multiple protein identifications (Supplementary Table 3).

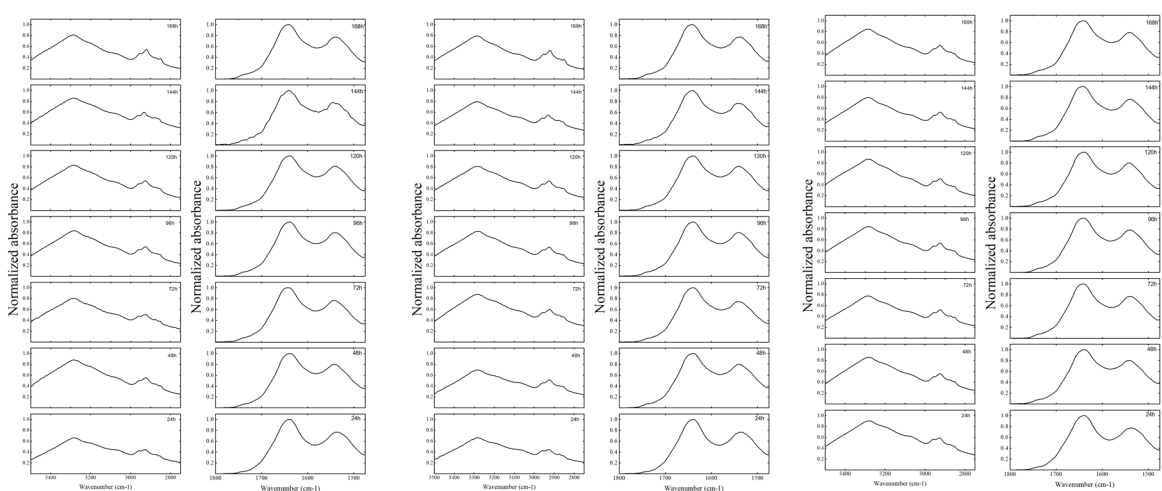
A wild type



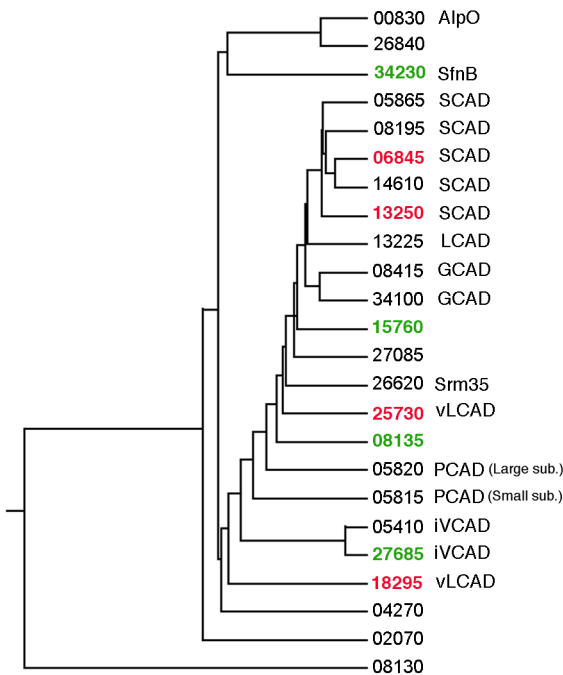
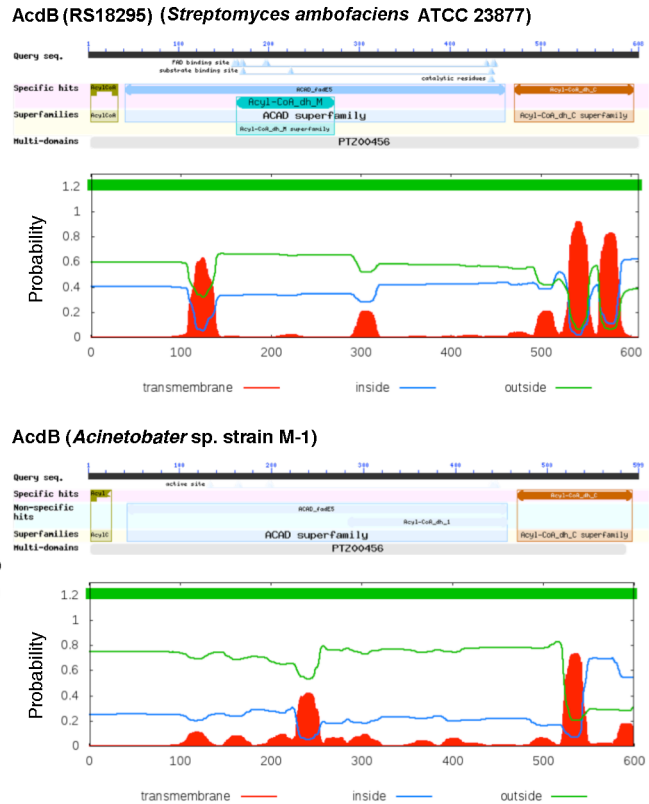
B *pirA*::pTYM-18



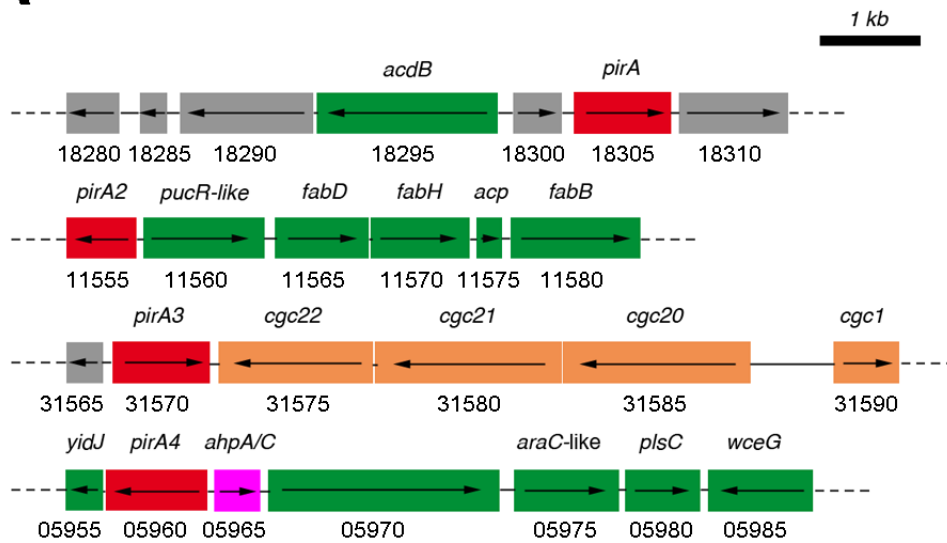
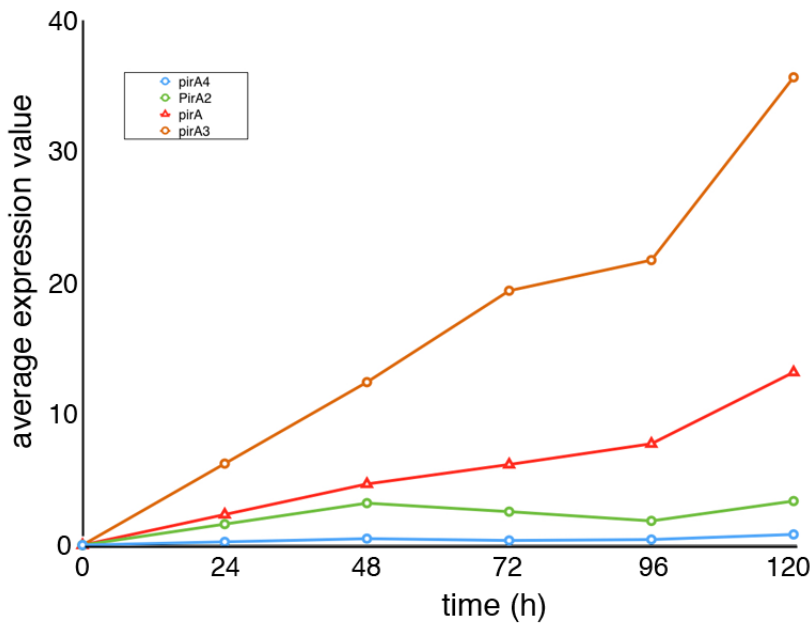
C *pirA*::pTYM-*pirA*



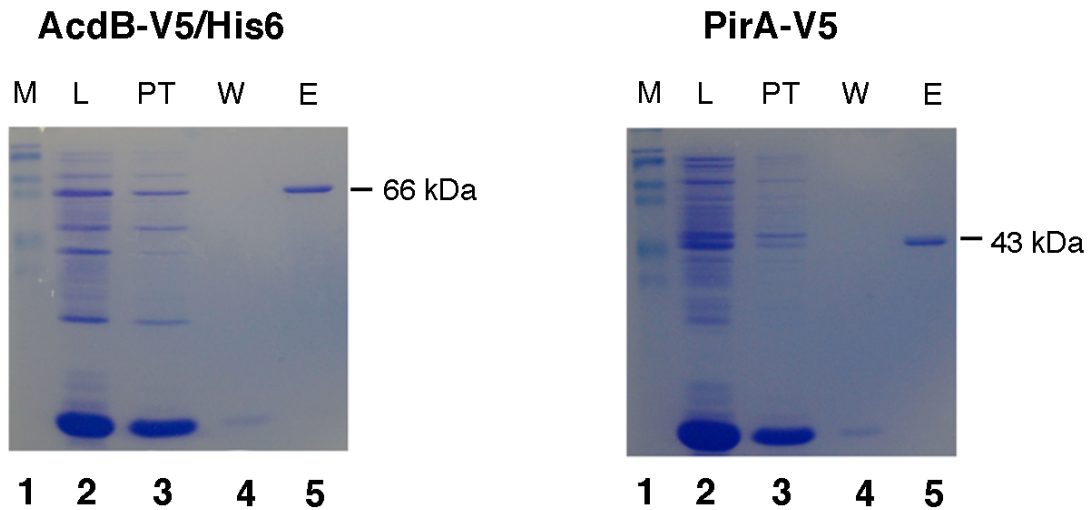
Supplementary Fig. 5. ATR-FTIR spectra of *S. ambofaciens* wild type (A) *pirA*::pTYM-18 (B) and *pirA*::pTYM-*pirA* (C) strains cultivated in YS broth and harvested at indicated time points.

A**B**

Supplementary Fig. 6. Cluster analysis of the *S. ambofaciens* ACADs and structural features of AcdB-3855. (A) Cluster analysis of deduced amino acid sequences of *S. ambofaciens* ACADs was carried out by ClusterW. Numbers refer to RefSeq (RS) number in the annotated genome sequence of *S. ambofaciens* ATCC 23877. ACAD-encoding genes that were up-regulated (red) or down-regulated (green) in *pirA*::pTYM-18 as compared to wild type strain are shown. Cluster analysis was refined by Conserved Domain database to deduce putative ACAD functions. SCAD, short-chain acyl-CoA dehydrogenase; LCAD, long-chain acyl-CoA dehydrogenase; vLCAD, very long-chain acyl-CoA dehydrogenase; GCAD, glutaryl-CoA dehydrogenase; PCAD, pimeloyl-CoA dehydrogenase; iVCAD, isovaleryl-CoA dehydrogenase; AlpO, alpomycin cluster-associated gene; Srm35, spiramycin cluster-associated gene; SfnB, ACAD with sulfate starvation induced SfnB domain. (B) Structural homologies between AcdB (RS18295) from *S. ambofaciens* ATCC 23877 and AcdB from *Acinetobacter* sp. strain M-1 as inferred from BLASTP-Conserved Domain (top) and TMMOD (bottom) analyses.

A**B**

Supplementary Fig. 7. Genetic map of the four *pirA*-containing loci of *S. ambofaciens*, and expression of *pirA* paralogs. (A) Genetic map of the four *pirA*-containing loci of *S. ambofaciens* ATCC 23877. Numbers refer to RefSeq (RS) number in the annotated genome sequence of *S. ambofaciens* ATCC 23877. (B) Expression of *pirA* paralogs (*pirA*, *pirA2*, *pirA3* and *pirA4*) in *S. ambofaciens* ATCC 23877 grown in YS broth at different time points, as inferred by RNAseq data.



Supplementary Fig. 8. Purification of recombinant AcdB-V5/His6 and pET-PirA-V5 proteins. SDS-PAGE analyses of crude extracts lysates (L) from *E. coli* BL21(DE3) competent cells transformed with either pET-AcdB-V5/His6 (lane 2, left) or pET-PirA-V5 (lane 2, right), respective pass-through fractions (PT) (lane 3, left and right), resin washing (W) (lane 4, left and right), and eluted (E) proteins (lane 5, left and right) are shown. Molecular mass ladders were run in parallel (lane 1, left and right). Molecular mass values of eluted proteins are reported on the right of each panel.

Table 1. List of the parent-daughter transitions used for quantification of CoA-related molecules.

	Retention time (min)	Parent ion [M+H]⁺	Quantifier ion [M-507]⁺
I.S. ([¹³ C ₃]-Malonyl-CoA)	1.4	857	350
Malonyl-CoA	1.4	854	347
Succinyl-CoA	2.1	868	361
Methylmalonyl-CoA	2.6	868	361
Acetyl-CoA	4.3	810	303
Acetoacetyl-CoA	4.5	852	345
Ethylmalonyl-CoA	4.9	882	375
Propionyl-CoA	7.5	824	317
Crotonyl-CoA	9.1	836	329
Butyryl-CoA	9.9	838	331